Title

Stochastic density functional theory combined with Langevin dynamics for warm dense matter

Journal

Physical Review E, 109(6)

ISSN

2470-0045

Authors

Hadad, Rebecca Efrat

Roy, Argha

Rabani, Eran

et al.

Publication Date

2024-06-01

DOI

10.1103/physreve.109.065304

Stochastic density functional theory combined with Langevin dynamics for warm dense matter

Rebecca Efrat Hadad
Fritz Haber Research Center for Molecular Dynamics, Institute of Chemistry, The Hebrew University of Jerusalem, 91904, Israel

Argha Roy
Institute for Physics, University of Rostock, 18051 Rostock, Germany

Eran Rabani
Department of Chemistry, University of California, Berkeley, California 94720, USA Materials Sciences Division, Lawrence Berkeley National Laboratory, Berkeley, California 94720, USA and The Raymond and Beverly Sackler Center of Computational Molecular and Materials Science, Tel Aviv University, Tel Aviv 69978, Israel

Ronald Redmer
Institute for Physics, University of Rostock, 18051 Rostock, Germany

Roi Baer
Fritz Haber Research Center for Molecular Dynamics, Institute of Chemistry, The Hebrew University of Jerusalem, 91904, Israel

This study overviews and extends a recently developed stochastic finite-temperature Kohn-Sham density functional theory to study warm dense matter using Langevin dynamics, specifically under periodic boundary conditions. The method's algorithmic complexity exhibits nearly linear scaling with system size and is inversely proportional to the temperature. Additionally, a novel linear-scaling stochastic approach is introduced to assess the Kubo-Greenwood conductivity, demonstrating exceptional stability for DC conductivity. Utilizing the developed tools, we investigate the equation of state, radial distribution, and electronic conductivity of Hydrogen at a temperature of 30,000K. As for the radial distribution functions, we reveal a transition of Hydrogen from gas-like to liquid-like behavior as its density exceeds 4 g/cm^3. As for the electronic conductivity as a function of the density, we identified a remarkable isosbestic point at frequencies around 7eV, which may be an additional signature of a gas-liquid transition in Hydrogen at 30,000K.

I. INTRODUCTION

Warm dense matter (WDM) exists in the interior of planets [1–10] and in brown dwarfs [11–15] and white dwarf stars [16, 17]. In inertial and fusion systems [18, 19], WDM is generated by subjecting materials to high-energy lasers [20]. Despite its significance, exploring the diverse forms and compositions of WDM poses a formidable challenge due to experimental complexities associated with preparing and sustaining materials under extreme conditions [5, 21, 22]. Consequently, computational methods have become indispensable for determining the equations of state as well as the chemical and physical properties of different systems.

Among these methods are ab initio molecular dynamics (AIMD) calculations [23–27], which rely on an "adiabatic" approximation. This approximation assumes that the quantum mechanical electrons reach thermal equilibrium under the applied temperature, electronic chemical potential, and Coulomb potentials corresponding to the instantaneous positions of the atomic nuclei. The latter then undergo classical motion under the conservative force derived from the electronic free energy, effectively acting as a potential of mean force (see, e.g., ref. [28]). The observables can be determined by averaging over a long adiabatic molecular dynamics (MD) trajectory.

The adiabatic and classical approximations behind AIMD have their limitations. There is evidence suggesting that a classical approximation may lack sufficient accuracy, particularly for temperatures below 1000K and under high pressures [29, 30]. Moreover, nonadiabatic effects, though often disregarded, as done here, have not been thoroughly explored in the context of AIMD in WDM. Previous studies of concerning nonadiabatic dynamics on metal surfaces introduce two distinct types of electron-nucleus forces in addition to the adiabatic one [31–34]. The first type manifests as rapid fluctuations resembling a stochastic process, while the second type involves dissipation, simulated as a friction force with a friction constant determined by the electronic structure. Since the molecular dynamics treats atomic nuclei as classical, the Langevin dynamics approach [28, 35] can be used to handle nonadiabatic effects, utilizing fluctuating-dissipating forces to impose the electronic temperature as the average value of the atomic nuclei kinetic energy in a canonical ensemble.

AIMD simulations for WDM need to consider both quantum Fermionic degeneracy and strong Coulomb in-

teractions [36]. The Kohn-Sham density functional theory (KS-DFT), which has proven highly successful as an ab initio theory for elucidating the structure of molecules and materials at zero temperature [25, 37–45], fulfills these requirements and has been extended to finite temperatures and has become a widely employed method for theoretical studies of WDM [46–51]. However, applying KS-DFT to WDM challenges calculating and storing an increasing number of Kohn-Sham eigenstates as the temperature rises. Consequently, for electronic temperatures exceeding 100,000K, other approaches, such as the extended KS method [52, 53] or "orbital-free DFT", which include finite temperature orbital free functionals [54–59] and method development [60–66] are preferred. Another emerging approach involves utilizing machine learning to generate potential-energy surfaces and interatomic forces based on KS-DFT and variational quantum Monte Carlo datasets. These learned models can then be employed in molecular dynamics calculations to predict material properties with reduced computational costs [67–71].

A linear scaling DFT procedure holds significant promise for investigating WDM, whether applied directly in AIMD or for generating training data sets for machine learning. This can be realized through stochastic DFT, as demonstrated by various authors in recent works [72–78]. In this paper, we elaborate on additional advancements in stochastic plane-waves Kohn-Sham density functional theory, integrating it with Langevin dynamics and introducing a novel approach for computing electronic conductivity. We thoroughly assess and benchmark the method, showcasing its practical application by conducting a detailed study of Hydrogen at 30,000K.

II. STOCHASTIC FINITE TEMPERATURE KOHN-SHAM DFT

A. Finite-temperature Kohn-Sham scheme

The combination of finite-temperature density functional theory [46, 79] and the Kohn-Sham procedure (FT-KS-DFT) [80] greatly simplifies the formidable problem of treating interacting electrons under the influence of a heat and electron bath. Under the FT-KS-DFT formalism, we need only study a system of non-interacting electrons in a one-body potential, which includes exchange-correlation contributions. As a result of the exchange-correlation potential, the non-interacting electron density is identical to that of the interacting system, and the grand potential of the interacting electron system can be expressed using the non-interacting grand potential together with exchange-correlation free-energy corrections. As the finite temperature diminishes towards zero, the FT-KS-DFT converges into the zero-temperature KS-DFT, with corresponding exchange-correlation contributions, and the free energy converges to zero-temperature ground-state energy [81].

To study infinite systems, it is beneficial to impose periodic boundary conditions within the simulation cell. The single electron wave functions of the non-interacting system are expressed as a linear combination of the plane wave basis $e^{i\boldsymbol{G}\cdot\boldsymbol{r}}$:

$$\psi\left(\boldsymbol{r}\right)=\sum_{\boldsymbol{G}}\tilde{c}_{\boldsymbol{G}}\frac{e^{i\boldsymbol{G}\cdot\boldsymbol{r}}}{\sqrt{\Omega}}, \tag{1}$$

where $\boldsymbol{G}=\frac{2\pi}{L}\left(m_x,m_y,m_z\right)$ is the simulation cell-commensurate wave vector and m_i integers. The wave vector parameter G_{cut} determines the size of the plane wave basis by requiring that $\|\boldsymbol{G}\|_2\leq G_{\mathrm{cut}}$. This cutoff identifies a subspace of dimension $D=\left[\frac{3\pi}{4}\left(\frac{L}{2\pi}G_{\mathrm{cut}}\right)^3\right]$ of the simulation cell's periodic functions, which is mapped by Eq. (1) onto the complex vector space of D-tuples $\mathbb{C}^D=\{\tilde{c}_{\boldsymbol{G}}\}_{\|\boldsymbol{G}\|_2\leq G_{\mathrm{cut}}}$. The basis truncation error can be systematically mitigated by increasing G_{cut}, or, equivalently the cutoff energy $E_{\mathrm{cut}}=\frac{\hbar^2G_{\mathrm{cut}}^2}{2m_e}$. Variational treatment of the finite-temperature Kohn-Sham equations within the subspace leads to a set of algebraic eigenvalue equations

$$\mathcal{H}\tilde{c}^{(j)}=\varepsilon_j\tilde{c}^{(j)},\quad j=1,2,\ldots,D \tag{2}$$

where $\mathcal{H}$ is the Kohn-Sham Hamiltonian (for more details on the representation, and the operators see, for example, ref. [38]) and ε_j and $\tilde{c}^{(j)}$ are its (real) eigenvalues and (complex) eigenvectors.

The electrons are in a grand canonical mixed state with temperature parameter $\beta=\left(k_BT\right)^{-1}$, where k_B is Boltzmann's constant, and chemical potential μ. The occupation of each single particle energy level ε is given by the Fermi-Dirac function $p_{\beta\mu}\left(\varepsilon\right)\equiv\left(1+e^{\beta(\varepsilon-\mu)}\right)^{-1}$. Correspondingly, the electron density can be expressed as a sum of level densities,

$$n\left(\boldsymbol{r}\right)=2\times\sum_j p_{\beta\mu}\left(\varepsilon_j\right)\left|\varphi_j\left(\boldsymbol{r}\right)\right|^2, \tag{3}$$

where

$$\varphi_j\left(\boldsymbol{r}\right)=\sum_{\boldsymbol{G}}\tilde{c}_{\boldsymbol{G}}^{(j)}\frac{e^{i\boldsymbol{G}\cdot\boldsymbol{r}}}{\sqrt{\Omega}} \tag{4}$$

are the (normalized, so that $\int_\Omega\left|\varphi_j\left(\boldsymbol{r}\right)\right|^2d\boldsymbol{r}=1$) Kohn-Sham eigenstates in real-space. The grand potential of the electrons is then given by [82]

$$\Phi_{\beta\mu}\left[n\right]\equiv U\left[n\right]-\beta^{-1}S_s\left[n\right]-\mu\int n\left(\boldsymbol{r}\right)d\boldsymbol{r}, \tag{5}$$

where

$$U\left[n\right]\equiv E_{\mathrm{orb}}-E_H\left[n\right]+\Phi_{\beta\mu,xc}\left[n\right]-\int v_{\beta\mu,xc}\left(\boldsymbol{r}\right)n\left(\boldsymbol{r}\right)d\boldsymbol{r} \tag{6}$$

is the Kohn-Sham energy. In Eq. (6),

$$E_{\mathrm{orb}}\equiv2\times\sum_j p_{\beta\mu}^j\varepsilon_j \tag{7}$$

is the orbital energy, $p^j_{\beta\mu} = p_{\beta\mu}(\varepsilon_j)$, $E_H[n]$ is the Hartree energy, and $\Phi_{\beta\mu,xc}[n]$ is the $\beta\mu$-dependent approximate exchange-correlation free energy functional of the density and $v_{\beta\mu,xc}(\boldsymbol{r}) = \frac{\delta\Phi_{\beta\mu,xc}}{\delta n(\boldsymbol{r})}$. While temperature-dependent exchange-correlation density functionals have been developed recently [83–88], in this paper we approximate $\Phi_{\beta\mu,xc}[n]$ by the zero temperature local density approximation (LDA, [80]) for the exchange correlation energy $E^{LDA}_{xc}[n]$ and correspondingly $v_{\beta\mu xc}(\boldsymbol{r})$ is approximated as the zero temperature LDA exchange-correlation potential $v^{LDA}_{xc}(\boldsymbol{r}) = \frac{\delta E^{LDA}_{xc}}{\delta n(\boldsymbol{r})}$. Finally, S_s in Eq. (5) is the entropy of non-interacting electrons at density $n(\boldsymbol{r})$ expressed as

$$S_s = -2 \times k_B \sum_j \left[p^j_{\beta\mu} \log p^j_{\beta\mu} + \bar{p}^j_{\beta\mu} \log \bar{p}^j_{\beta\mu} \right], \qquad (8)$$

where, in brevity, $\bar{p}^j_{\beta\mu} \equiv 1 - p^j_{\beta\mu}$. In this Kohn-Sham procedure we find the density $n(\boldsymbol{r})$ that minimizes the grand potential $\Phi_{\beta\mu}$. The number of electrons is $\tilde{N}_e(\mu) = \left(\frac{\partial \Phi_{\beta\mu}}{\partial \mu}\right)_\beta = 2 \times \sum_j p^j_{\beta\mu}$.

The ξ-component ($\xi = 0, 1, 2$ indicates respectively x, y, z) of the force on an atomic nucleus A ($A = 0, \ldots, N_n - 1$, where N_n is the number of atomic nuclei in the simulation cell) is equal to the corresponding derivative of the grand potential, $F^i = -\frac{\partial \Phi_{\beta\mu}}{\partial R_i} + F^{NN}_i$, where $i \equiv (3A + \xi)$ is the force index, and F^{NN}_i is the sum of forces exerted by all other atomic nuclei. This force is an average force over all ground and excited electronic states of all possible charge states of the system.

An alternative to working in the grand canonical ensemble, where μ is given, is to impose a fixed average number of electrons N_e and then tune μ accordingly. Such an ensemble is more natural for small, finite simulation cells. In this ensemble the chemical potential becomes a function of the imposed value of N_e, denoted $\tilde{\mu}(N_e)$, defined implicitly by solving the equation

$$N_e = 2 \times \sum_j p^j_{\beta\tilde{\mu}(N_e)}. \qquad (9)$$

In this ensemble we find the density $n(\boldsymbol{r})$ that minimizes the Helmholtz free energy $\mathcal{F}_{\beta N_e} = U - \beta^{-1} S_s$ and the force is its derivative, $F_i = -\frac{\partial \mathcal{F}_{\beta N_e}}{\partial R_i} + F^{NN}_i$. Once again, this force is an average over all ground and excited electronic states of all possible charge states of the system.

Regardless of the ensemble used, the electronic force component i is obtained from the electron density and the corresponding derivative of the electron-nucleus force potential:

$$F_i = -\int n(\boldsymbol{r}) \frac{\partial}{\partial R_i} v_{\mathrm{eN}}(\boldsymbol{r})\, d\boldsymbol{r} + F^{NN}_i,$$

and when non-local pseudopotentials are employed, i.e., $\hat{v}_{\mathrm{eN}} = v_{\mathrm{loc}}(\boldsymbol{r}) + \hat{v}_{nl}$ the following generalization needs be used (now in vector notation):

$$\boldsymbol{F} = -2 \times \sum_j p^j_{\beta\mu} \langle \varphi_j | \boldsymbol{\nabla} \hat{v}_{\mathrm{eN}} | \varphi_j \rangle + \boldsymbol{F}^{NN}. \qquad (10)$$

B. The stochastic density functional approach

Stochastic density functional theory [72] is based on the concept of random wave functions

$$\eta(\boldsymbol{r}) \equiv \sum_{\boldsymbol{G}} \tilde{\eta}^{\boldsymbol{G}} \frac{e^{i\boldsymbol{G}\cdot\boldsymbol{r}}}{\sqrt{\Omega}} \qquad (11)$$

in which the random coefficients $\tilde{\eta}^{\boldsymbol{G}}$ are given, in vector notation, by operating with the square-root Fermi-Dirac operator $\sqrt{p_{\beta\mu}(\mathcal{H})}$ on a random vector:

$$\tilde{\eta} \equiv \sqrt{p_{\beta\mu}(\mathcal{H})}\tilde{\chi} \qquad (12)$$

where $\tilde{\chi}$ is a random vector with components $\tilde{\chi}^{\boldsymbol{G}} \equiv e^{i\theta_{\boldsymbol{G}}}$, where $\theta_{\boldsymbol{G}}$ are independent random phases (between 0 and 2π). It is straightforward to check that

$$\mathrm{E}\left[\tilde{\chi}^{\boldsymbol{G}'} \tilde{\chi}^{\boldsymbol{G}*}\right] = \delta_{\boldsymbol{G}'\boldsymbol{G}}. \qquad (13)$$

Here, the symbol $\mathrm{E}[r]$ is the expected value of a random variable r. The random variable $\tilde{\eta}^{\boldsymbol{G}'} \tilde{\eta}^{\boldsymbol{G}*}$ is an unbiased estimator of the KS density matrix in G-space, relying on the following exact identity $[p_{\beta\mu}(\mathcal{H})]_{\boldsymbol{G}'\boldsymbol{G}} = \mathrm{E}\left[\tilde{\eta}^{\boldsymbol{G}'} \tilde{\eta}^{\boldsymbol{G}*}\right]$. This relation is proved by plugging Eq. (12) on the right hand side and using Eq. (13). Similarly, sampling $\eta(\boldsymbol{r})\,\eta(\boldsymbol{r}')^*$, where $\eta(\boldsymbol{r})$ is defined in Eq. (11), provides an estimate for the KS density matrix $\rho(\boldsymbol{r}, \boldsymbol{r}') = 2 \times \sum_j p_{\beta\mu}(\varepsilon_j)\, \varphi_j(\boldsymbol{r})\, \varphi_j(\boldsymbol{r}')^*$. From this, $|\eta(\boldsymbol{r})|^2$ is an unbiased estimator for the electron density $n(\boldsymbol{r})$, relying on the exact identity:

$$n(\boldsymbol{r}) = 2 \times \mathrm{E}\left[|\eta(\boldsymbol{r})|^2\right]. \qquad (14)$$

This expression is the essence of stochastic KS-DFT: it replaces the *calculation* of the electron density $n(\boldsymbol{r})$ (Eq. (3)), which requires the KS-DFT eigenstates and eigenvalues (Eq. (2)) by a statistical sampling of the random variable $|\eta(\boldsymbol{r})|^2$.

The fact that the expected value of the absolute square of the random variable $\eta(\boldsymbol{r})$ gives the density, means that we can now use sampling methods to obtain actual estimates of the density. If we produce a sample of I independent random vectors $\tilde{\chi}_i$ ($i = 1, \ldots, I$) and from them, using Eqs. (11)-(12) obtain samples of $\eta_i(\boldsymbol{r})$ then the density can be estimated as an average

$$n(\boldsymbol{r}) = 2 \times \frac{1}{I} \sum_{i=1}^{I} \left[|\eta_i(\boldsymbol{r})|^2\right].$$

This sampling procedure is straightforward to parallelize using distributed memory model, for example, the message-passing-interface library. Observables, such as the forces on atomic nuclei, can be expressed as stochastic traces as well (see subsection III). From statistics, the fluctuations in the density or forces are proportional to the inverse square root of the sample size. For the calculations shown below we used a sample of $I = 40$ stochastic orbitals (irrespective of the system size).

C. Chebyshev expansion methods

1. The essential Chebyshev expansion

We now describe a recipe for performing calculations of the type shown in Eq. (12), i.e. operating with a function of the Hamiltonian, namely $z(\mathcal{H})$ on some given a vector χ: $|\zeta\rangle = z(\mathcal{H})|\chi\rangle$. For this, we use the Chebyshev expansion [89] of length N_C, $\zeta^{\boldsymbol{G}} = \sum_{n=0}^{N_C-1} Z^{(n)} \chi_n^{\boldsymbol{G}}$, which we write in ket-form as:

$$|\zeta\rangle = \sum_{n=0}^{N_C-1} Z^{(n)} |\chi_n\rangle . \tag{15}$$

The Chebyshev coefficients are defined by

$$Z^{(n)} = \frac{2}{N_C} e^{i\frac{\pi}{N_C}n} \tilde{z}^{(n)}$$

where the series $\left\{\tilde{z}^{(n)}\right\}_{n=0}^{N_C-1}$is the discrete Fourier transform of $\left\{z\left(\bar{E} + \Delta E \times \cos\left(\frac{l+\frac{1}{2}}{N_C}\pi\right)\right)\right\}_{l=0}^{N_C-1}$. In the last expression, $\bar{E} = (E_{max} + E_{min})/2$, $\Delta E = (E_{max} - E_{min})/2$ and E_{min} (E_{max}) is a lower (upper) bound estimate to the smallest (largest) eigenvalue of $\mathcal{H}$.

The expansion length N_C is chosen to be sufficiently large so that the $\left|Z^{(n)}\right|$ are all smaller than a threshold value 10^{-d}, (typically $d = 7$ or 8) for $n > N_C$. An estimate for the Chebyshev length is the following expression:

$$N_C \approx \frac{3d}{4} \times \beta \times \Delta E. \tag{16}$$

The Chebyshev vectors $|\chi_n\rangle$ in Eq. (15) are defined as $|\chi_n\rangle \equiv T_n(\mathcal{H}_s)|\chi\rangle$, where $T_n(x)$ is the n^{th} Chebyshev polynomial [90] and $\mathcal{H}_s \equiv \frac{\mathcal{H}-\bar{E}}{\Delta E}$ is the shifted-scaled Hamiltonian, having all eigenvalues in the interval $[-1, 1]$. Based on a recurrence formula between any three consecutive Chebyshev polynomials [90], the Chebyshev vectors χ_n can be computed iteratively (hence only three of them are needed at a given time):

$$|\chi_n\rangle = 2\mathcal{H}_s|\chi_{n-1}\rangle - |\chi_{n-2}\rangle , \quad n \geq 2,$$

The first two vectors are given by:

$$|\chi_0\rangle = |\chi\rangle , \qquad |\chi_1\rangle = \mathcal{H}_s|\chi_0\rangle ,$$

2. Operating with several functions of $\mathcal{H}$ on a given state $|\chi\rangle$

Each term in the Chebyshev expansion of Eq. (15) is a product of a Chebyshev coefficient Z^n and a Chebyshev vector $|\chi_n\rangle$. The former depends on the function $z(\mathcal{H})$, while the latter does not. Suppose we want to operate with several different functions $z_m(\mathcal{H})$ $(m = 1, 2, \ldots, M)$ on the *same* vector χ:

$$|\zeta_m\rangle = z_m(\mathcal{H})|\chi\rangle .$$

Chebyshev expansions can calculate these vectors

$$|\zeta_m\rangle = \sum_{n=0}^{N_C-1} Z_m^{(n)} |\chi_n\rangle , \tag{17}$$

where $Z_m^{(1)}$, $Z_m^{(2)}$, ... are the coefficients corresponding to the function $z_m(\varepsilon)$. Most of the numerical effort goes into computing the vectors $|\chi_n\rangle$ and these are shared by all the different evaluations in Eq. (17). Therefore, there is but a minute overhead in the effort to calculate M $|\zeta_m\rangle$s relative to just one $|\zeta\rangle$.

3. Energy windows

An example of using this approach is the *Energy Windows* method [91]. Here, we define N_w chemical potentials

$$\mu_{N_w} \equiv \mu \geq \mu_{N_w-1} \geq \cdots \geq \mu_1$$

and corresponding energy window projections

$$z_m(\mathcal{H}) = \sqrt{p_{\beta\mu_m} - p_{\beta\mu_{m-1}}}, \qquad m = 2, \ldots, N_w$$
$$z_1(\mathcal{H}) = \sqrt{p_{\beta\mu_1}}.$$

Each of these functions projects a different energy range between the chemical potentials. The sum of the square of these functions yields the Fermi-Dirac projector

$$p_{\beta\mu}(\mathcal{H}) = z_{N_w}(\mathcal{H})^2 + z_{N_w-1}(\mathcal{H})^2 + \cdots + z_1(\mathcal{H})^2 .$$

Therefore, for any one-body operator $\mathcal{A}$, the KS expectation value $\langle\mathcal{A}\rangle \equiv \mathrm{Tr}\left[p_{\beta\mu}(\mathcal{H})A\right]$ can be written as a sum of contributions from differing energy windows:

$$\langle\mathcal{A}\rangle = \sum_{m=1}^{N_w} \mathrm{Tr}\left[z_m(\mathcal{H})Az_m(\mathcal{H})\right] .$$

The equivalent stochastic expression is

$$\langle\mathcal{A}\rangle = \sum_{m=1}^{N_w} \mathrm{E}\left[\langle\zeta_m|\mathcal{A}|\zeta_m\rangle\right] .$$

Depending on the observable $\mathcal{A}$, this procedure helps reduce the fluctuations in estimating $\langle\mathcal{A}\rangle$ since ζ_m and $\zeta_{m'}$ span largely non-overlapping energy windows.

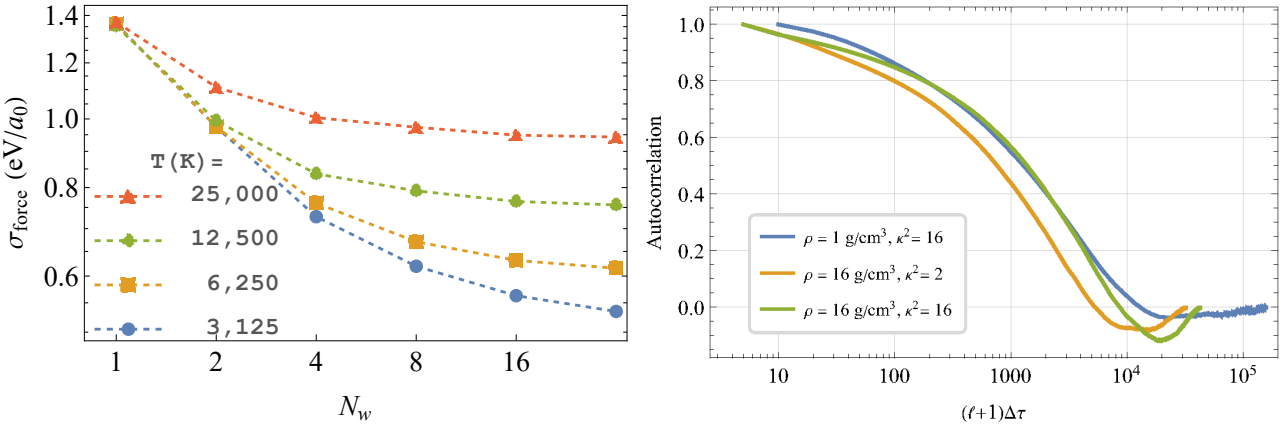

Figure 1. **Left panel**: The sDFT force standard deviation $\sigma_f \equiv \sqrt{\frac{1}{3N_H}\text{Tr}\Sigma_\phi^2}$ (per degree of freedom) for selected electronic temperatures as a function of the number of windows N_w in H_{128} at $\rho = 1\,g/cm^3$. **Right panel**: The instantaneous position autocorrelation $C_R(\ell)$ (see Eq. (25), averaged over all atoms) during a $T = 30,000K$ Langevin trajectory of H_{256} in two densities with additional white noise force (given in terms of κ, see Eq. (23)) and a time step of $\Delta t = 5\,\hbar E_h^{-1}$ for $\rho = 16\,g/cm^3$ and $\Delta t = 10\,\hbar E_h^{-1}$ for $\rho = 1\,g/cm^3$.

In the left panel of Fig. 1, we show the standard deviation of the electronic force on the atomic nuclei (per degree of freedom) as a function of the number of windows for selected temperatures. It is seen that for low temperatures this standard deviation is reduced by as much as a factor of 2 as N_W reaches 16 or 32. However, for the high temperature considered, the windows are less efficient, reducing the standard deviation by, at most, a factor of 1.4.

4. *Chebyshev moments*

A Chebyshev moment M_n is the *trace* of a Chebyshev polynomial $T_n(\mathcal{H}_s)$. The overlap $\langle\chi|\chi_n\rangle$ is an unbiased estimator of M_n, based on the identity $\text{Tr}[T_n(\mathcal{H}_s)] = \text{E}[\langle\chi|T_n(\mathcal{H}_s)|\chi\rangle]$, or:

$$M_n = \text{E}[\langle\chi|\chi_n\rangle].$$

Knowledge of the moments allows us to compute the trace of any function $z(\mathcal{H})$ of the KS Hamiltonian $\mathcal{H}$ through the formula:

$$\text{Tr}[z(\mathcal{H})] = \sum_{n=0}^{N_C-1} Z^{(n)} M_n,$$

where $Z^{(n)}$ are the coefficients for the Chebyshev expansion of the function $z(\varepsilon)$.

Examples where moments are useful:

1. When working in the canonical ensemble mentioned above, with a fixed number of electrons N_e, the chemical potential μ is a function of N_e defined implicitly by Eq. (9), depending on the KS eigenvalues ε_j. However, in sDFT, we do not have access to ε_j. Hence, we use the Chebyshev Moments to develop an alternative implicit equation for μ:

$$N_e = 2 \times \sum_{n=0}^{N_C-1} P^{(n)}_{\beta\mu(N_e)} M_n, \tag{18}$$

where the $P^{(n)}_{\beta\mu}$s are the Chebyshev coefficients corresponding to $p_{\beta\mu}(\varepsilon)$. The actual determination of μ uses a numerical root-searching algorithm (e.g., the bisection method) applied to Eq. (18). The search for μ is a speedy step since the Chebyshev moments are independent of μ, so they are calculated only once and then stored while calculating the Chebyshev coefficients $P_{\beta\mu}$ any value of μ only involves a single fast Fourier transform.

2. The non-interacting electron entropy of Eq. (8) is estimated as

$$S_s = 2 \times \sum_{n=0}^{N_C-1} S^{(n)}_{\beta\mu} M_n, \tag{19}$$

where $S^{(n)}_{\beta\mu}$ are the Chebyshev coefficients corresponding to the function $s_{\beta\mu}(\varepsilon) = -\left(p_{\beta\mu}(\varepsilon)\log p_{\beta\mu}(\varepsilon) + \bar{p}_{\beta\mu}(\varepsilon)\log\bar{p}_{\beta\mu}(\varepsilon)\right)$.

3. The orbital energy E_{orb} of Eq. (7) is estimated as

$$E_{\text{orb}} = 2 \times \sum_{n=0}^{N_C-1} E^{(n)}_{\beta\mu} M_n,$$

where the $E^{(n)}_{\beta\mu}$ are the Chebyshev coefficients corresponding to $e_{\beta\mu}(\varepsilon) = p_{\beta\mu}(\varepsilon)\,\varepsilon$.

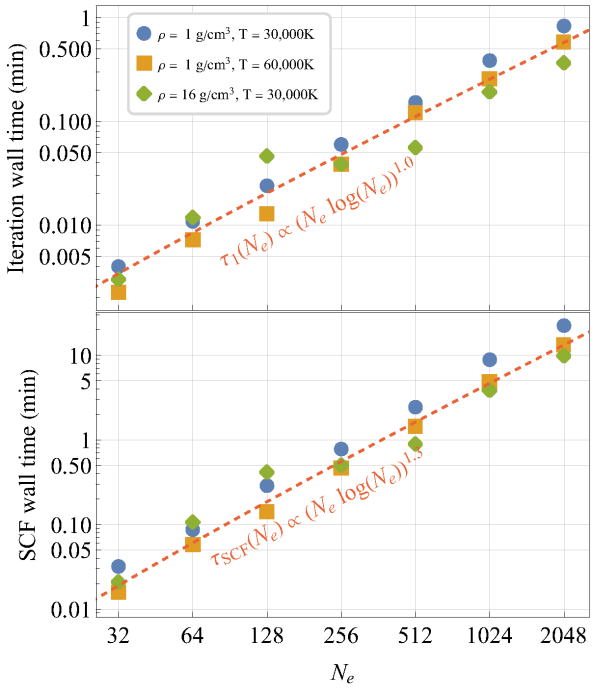

Figure 2. The self-consistent-field (SCF) wall times as a function of the number of electrons N_e for Hydrogen at the specified densities and temperatures. **Top panel**: a single SCF iteration; **Bottom panel**: the entire SCF calculation (stopped when the changes in energy per electron are below $10^{-5}E_h$). The calculations used the cutoff energy of $E_{\rm cut} = 9E_h$, 40 stochastic orbitals and a *single core per stochastic orbital* on our Core-i7 cluster.

D. Performance of the sDFT calculation

Fig. 2 shows the wall time self-consistent calculations (averaged over many sDFT Langevin dynamics steps) as a function of the number of electrons N_e in the simulation cell for Hydrogen at specified densities and temperatures. The computation time of a single cycle of an SCF calculation scales linearly in $x = N_e \log N_e$. Since the number of SCF cycles required to converge to a given criterion grows mildly with system size, the overall scaling is $x^{1.3}$. Calculations with higher temperatures and the same number of electrons N_e are faster since the Chebyshev expansions shorten in inverse proportion to temperature (see Eq. (16)). Higher density calculations with the same number of atoms N_e also require less computation time because of the smaller simulation cell sizes.

Let us discuss the wall times and their dependence on scale the cutoff energy $E_{\rm cut}$. The plane wave basis size is determined by the volume in G-space of the highest momentum vector $G_{max} = \sqrt{\frac{2m_e}{\hbar^2}E_{\rm cut}}$ (where m_e is the electron mass and $\hbar$ is Planck's constant) and therefore proportional to $E_{\rm cut}^{3/2}$. In addition, the length of the Chebyshev expansion is proportional to $E_{\rm cut}$ (see Eq. (16)). Hence, overall, the wall time scales steeply as $E_{\rm cut}^{5/2}$, i.e., wall time increases by a factor 32 every time the cutoff energy increases by a factor 4.

We have not yet developed a capability to expedite the calculation speed for each stochastic orbital. We can achieve high factors if we use a GPU on each node for this purpose.

III. STOCHASTIC FORCES AND LANGEVIN DYNAMICS

In the previous section, we discussed the WDM's electronic structure at inverse temperature β. In this section we concentrate more on the behavior of the atomic nuclei in WDM. At thermal equilibrium their state is canonically distributed with a temperature identical to that of the electrons. Here we discuss how we use the method of Langevin dynamics to estimate the expected value of various observables concerning atomic nuclei within the canonical ensemble.

A. Regularization of the stochastic forces

In sDFT, the force on each atomic nucleus is a vector of a random variable components [72]:

$$\boldsymbol{f} = -2 \times \langle \eta \,|\boldsymbol{\nabla}\hat{v}_{\rm eN}|\, \eta \rangle + \boldsymbol{F}^{NN} \tag{20}$$

where $\eta(\boldsymbol{r})$ is defined in Eq. (11) and $\boldsymbol{F}^{NN}$ is the force due to the other bare atomic nuclei. Using the stochastic trace formula, the force $\boldsymbol{F}$ of Eq. (10) is the expected value of the random force:

$$\boldsymbol{F} = \mathrm{E}\left[\boldsymbol{f}\right].$$

The $3N_n \times 3N_n$ symmetric positive-definite force covariance matrix is $\left(\Sigma_f^2\right)_{ii'} = \mathrm{E}\left[f_i f_{i'}\right] - F_i F_{i'}$, or, in matrix notation

$$\Sigma_f^2 \equiv \mathrm{E}\left[\boldsymbol{f}\boldsymbol{f}^T\right] - \boldsymbol{F}\boldsymbol{F}^T. \tag{21}$$

To ease the handling of stochastic forces, we add independent white noise $\boldsymbol{\zeta}$ ($\mathrm{E}\left[\boldsymbol{\zeta}\right] = 0$):

$$\boldsymbol{\varphi} = \boldsymbol{f} + \boldsymbol{\zeta}. \tag{22}$$

The covariance matrix $\mathrm{E}\left[\boldsymbol{\zeta}\boldsymbol{\zeta}^T\right]$ of this additional white noise is specially constructed to allow the covariance $\Sigma_{\boldsymbol{\varphi}}^2$ of the total force to be uniform, i.e. a *multiple of the unit matrix*:

$$\Sigma_{\boldsymbol{\varphi}}^2 \equiv \mathrm{E}\left[\boldsymbol{\varphi}\boldsymbol{\varphi}^T\right] - \boldsymbol{F}\boldsymbol{F}^T = \sigma^2 \mathrm{I} = \kappa^2 \sigma_f^2 \mathrm{I}, \tag{23}$$

where σ^2 is larger ($\kappa \geq 1$) than the largest eigenvalue σ_f^2 of Σ_f^2. The white noise force ζ is thus sampled, using the Metropolis-Hastings algorithm, to have a Gaussian distribution with the positive-definite covariance matrix

$\Sigma_\zeta^2 \equiv \sigma^2 I - \Sigma_f^2$. The procedure obviously requires an estimate of the sDFT force covariance Σ_f^2 and we use a sample of N_s force vectors to estimate it (with $N_s = 50$, seemingly quite sufficient). The covariance estimate is done once every N_j MD steps (we took $N_j = 150$). A force having such a uniform covariance matrix enables using the same friction coefficient for all degrees of freedom, and therefore simplifies the temperature control in the Langevin dynamics calculation.

B. The stochastic Langevin equations of motion

The stochastic force $\boldsymbol{\varphi}(\boldsymbol{R})$ for a given atomic nuclei configuration is now used to perform Langevin molecular dynamics from which we obtain configuration and momentum samples that are canonically distributed. From these samples we can compute the thermodynamic properties of the system. The dynamics involves solving the Langevin equation of motion

$$\begin{aligned}\dot{\boldsymbol{P}}(t) &= \boldsymbol{\varphi}(\boldsymbol{R}(t)) - \gamma \boldsymbol{P}(t),\\ \dot{\boldsymbol{R}}(t) &= M^{-1}\boldsymbol{P}(t),\end{aligned}$$

where M^{-1} is a diagonal matrix of the inverse nuclei mass, and γ is the diagonal matrix of friction coefficients. We use a time-discretized solver [92] for the stochastic differential equation, from which we obtain a discretized trajectory of N_T atomic configurations $\boldsymbol{R}^{(n)} = \boldsymbol{R}(n\Delta\tau)$ $(n = 1, \ldots, N_T)$ and their momenta $\boldsymbol{P}^{(n)} = \boldsymbol{P}\left(\left(n - \frac{1}{2}\right)\Delta\tau\right)$, where $\Delta\tau$ is the time step. The phase-space trajectory is built from the following evolution steps

$$\begin{aligned}\boldsymbol{P}^{(n+1)} &= e^{-\gamma\Delta\tau}\boldsymbol{P}^{(n)} + \left(\frac{1 - e^{-\gamma\Delta\tau}}{\gamma}\right)\boldsymbol{\varphi}\left(\boldsymbol{R}^{(n)}\right),\\ \boldsymbol{R}^{(n+1)} &= \boldsymbol{R}^{(n)} + M^{-1}\boldsymbol{P}^{(n+1)}\Delta\tau,\end{aligned}$$

and in the limit $\Delta\tau \to 0$ a Langevin trajectory is obtained. Here, the (diagonal) friction matrix γ is determined from the fluctuation-dissipation relation, which is given by

$$\sigma^2 = \frac{\gamma\Delta\tau/2}{\tanh(\gamma\Delta\tau/2)} \times \frac{2\gamma M}{\beta}. \tag{24}$$

C. Statistical sampling

For sufficiently small $\Delta\tau$ each of the trajectory configurations $\boldsymbol{R}^{(n)}$ is equivalent to a sample taken from the Boltzmann distribution $p_\beta^B(\boldsymbol{R}) \propto e^{-\beta V_{BO}(\boldsymbol{R})}$ where $V_{BO} \equiv \Phi_{\beta\mu} + E_{NN}$ $(V_{BO} = \mathcal{F}_{\beta N_e} + E_{NN})$ is the *electronic* grand-canonical (canonical) potential (see Eq. (5)). The momentum $\boldsymbol{P}^{(n)}$ is equivalent to a sample from the Maxwell-Boltzmann probability distribution function $p_{R\beta}^{MB}(\boldsymbol{P}) \propto e^{-\beta\sum_{i=1}^{N_N}\frac{\boldsymbol{P}_i^2}{2M_i}}$.

The estimate for the thermal average $\langle O\rangle_\beta \equiv \iint O(\boldsymbol{R},\boldsymbol{P})\, p_\beta^B(\boldsymbol{R})\, d\boldsymbol{R}\, p_\beta^{MB}(\boldsymbol{P})\, d\boldsymbol{P}$ of a given observable $O(\boldsymbol{R},\boldsymbol{P})$ is simply the sample mean $\bar{O} \equiv \frac{1}{N_T}\sum_{n=1}^{N_T} O^{(n)}$ over the sequence $O^{(n)} \equiv O\left(\boldsymbol{R}^{(n)}, \boldsymbol{P}^{(n)}\right)$. The sample variance $\overline{\Delta O^2} = \frac{1}{N_T}\sum_{n=1}^{N_T}\Delta O^{(n)}$, where $\Delta O^{(n)} = O^{(n)} - \bar{O}$, allows us to determine a confidence interval for the thermal average. For example, the 70% confidence interval is $\left[\bar{O} - \delta O, \bar{O} + \delta O\right]$ where $\delta O \equiv \sqrt{\frac{1}{N_{\rm ind}}\overline{\Delta O^2}}$and $N_{\rm ind}$ is the number of statistically independent samples in the sequence $O^{(n)}$. If the values $O^{(1)}$, $O^{(2)}$, ... were uncorrelated then $N_{\rm ind}$ would be just the sample size N_T. However, because the configurations $\boldsymbol{R}^{(n)}$ are part of a *molecular dynamics trajectory*, $O^{(n+1)}$ is *correlated* with $O^{(n)}$, and $O^{(n+2)}$ is correlated with $O^{(n+1)}$, etc. and therefore $N_{ind} < N_T$. It is common to quantify the strength of this correlation using *the auto-correlation function* for O, defined by $C_O(\ell\Delta\tau) \equiv \frac{\left\langle \Delta O^{(n)}\Delta O^{(n+\ell)}\right\rangle}{\left\langle \Delta O^{(n)2}\right\rangle}$ (the expression on the right-hand side is independent of n). In a given sample trajectory, the auto-correlation function is estimated by

$$C_O(\ell\Delta\tau) \approx \frac{\sum_n \Delta O^{(n)}\Delta O^{(n+\ell)}}{\sum_n \Delta O^{(n)2}}. \tag{25}$$

It starts with the value $C_O(0) = 1$ (full correlation) and then decays steadily as step separation ℓ grows until hitting a regime of small random fluctuations. The decay is characterized by a correlation time τ_O, for which $C_O(\tau_O) = e^{-1}$. We also define the *correlation length* $\ell_O = \frac{\tau_O}{\Delta\tau}$. We view ℓ_O consecutive samples as "correlated" while later samples are considered *uncorrelated*. The number of *effectively independent* samples is thus estimated as: $N_{\rm ind} \approx N_T/\ell_O$. In the right panel of Fig. 1 we show the Langevin dynamics position autocorrelation function $C_R(\ell\Delta\tau)$ of hydrogen at $T = 30,000K$, for two densities ρ and two white noise parameters κ^2 (see Eq. (23)). The correlation times τ_R are weakly dependent on the density but grow significantly with κ. Hence, we strive for small values of $\kappa^2 > 1$.

D. Computational demonstration of μVT - N_eVT ensemble equivalence

Fig. 3 displays time-dependent values of selected observables in two Langevin dynamics trajectories of hydrogen at mass density $\rho = 1\, g \times cm^{-3}$ at $T = 30,000K$. The two trajectories are calculated in different electronic ensembles: the left panel of the plot shows the results of an N_eVT-like ensemble, where we impose a constant electron number $N_e = 128$ at each time step by tuning the electronic chemical potential $\tilde{\mu}\left(N_e; \boldsymbol{R}^{(n)}\right)$ in the Fermi-Dirac function at each time step (see Eq. (9)). This chemical potential fluctuates in time, as do the positions and momenta of the atomic nuclei. The right

panel shows the results of an μVT ensemble, where the electronic chemical potential is set to a constant value of $\mu = 9.56\,eV$. Now the number of electrons fluctuate but *on average* it is 128. The observables are the kinetic energy per atomic degree of freedom $T^{(n)}$ (divided by k_B and given in kilo-Kelvin), the pressure $P^{(n)}$, the chemical potential $\tilde{\mu}^{(n)}$, the Helmholtz energy $\tilde{\mathcal{F}}^{(n)}_{\beta N_e}$, in the left panel, the electron number $\tilde{N}_e^{(n)}$ and the Grand potential $\tilde{\Phi}^{(n)}_{\beta\mu}$ in the right panel. Upon studying the numerical results in Fig. 3, it is obvious that the average over the fluctuating chemical potential on the left panel $\langle\tilde{\mu}\rangle_{N_eVT} = \frac{1}{N_T}\sum_{n=1}^{N_T}\tilde{\mu}\left(N_e;\boldsymbol{R}^{(n)}\right)$ is very similar to the constant chemical potential μ imposed in the μVT ensemble on the right panel. Similarly, the average over the fluctuating number of electrons on the right panel $\left\langle\tilde{N}_e\right\rangle_{\mu VT} = \frac{1}{N_T}\sum_{n=1}^{N_T}\tilde{N}_e\left(\mu;\boldsymbol{R}^{(n)}\right)$ is very close to the imposed number of electrons N_e used in the N_eVT ensemble on the left panel. These results can be summarized in the following relation:

$$\mu = \langle\tilde{\mu}\rangle_{N_eVT} \Leftrightarrow N_e = \left\langle\tilde{N}_e\right\rangle_{\mu VT},$$

showing that in our finite-sized system, the two ensembles μVT and N_eVT are already equivalent, which is characteristic of the thermodynamic limit. All calculations shown in the next section were performed in the N_eVT ensemble.

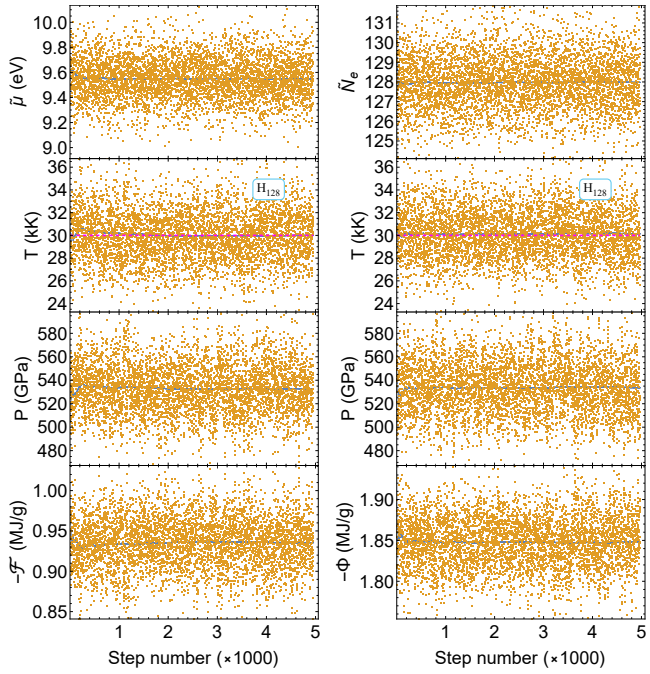

Figure 3. The instantaneous values (brown) and running averages (blue) of observables in two Langevin molecular dynamics trajectories of H_{128} (at mass density of $\rho = 1\mathrm{g}\times\mathrm{cm}^{-3}$ and target temperature of 30,000K): on the **left panel**, the NVT-like trajectory, where the number of electrons is fixed ($N_e = 128$) by tuning the chemical potential $\tilde{\mu}^{(n)}$ at each time step (see Eq. (9)). On the **right panel**, the μVT trajectory, where the chemical potential is fixed ($\mu = 9.56\,\mathrm{eV}$) while the number of electrons $\tilde{N}_e^{(n)}$ fluctuates. Details of the Langevin dynamics: the white noise fluctuation is $\sigma = 4\sigma_f$, i.e. $\kappa = 4$ (see Eq. (23)), the time step is $\Delta\tau = 10\,\mathrm{atu}$, and the sDFT force covariance (see Eq. (21)) is calculated using 50 independent samples once every 150 dynamical time steps.

IV. KUBO-GREENWOOD CONDUCTIVITY

In this section, we consider the stochastic calculation of the Kubo-Greenwood conductivity [93, 94]. In the context of WDM, these calculations were addressed in refs. [95, 96] but they become demanding as the system size and temperature increase. Hence, a stochastic calculation may be preferable for such systems as discussed in Ref. [74]. Here, we provide an improved approach including the DC conductivity with considerably lower statistical errors. We also provide a detailed description of the theory, the derivation, and how the calculations were made.

Kubo's analysis [93] starts with expressing the complex conductivity

$$\sigma_{\xi\xi'}(\omega) = \int_0^\infty \phi_{\xi\xi'}(t)\, e^{-i\omega t}dt, \tag{26}$$

as the Fourier transform of the dipole-current-density response function:

$$\phi_{\xi\xi'}(t) = \frac{1}{i\hbar}\mathrm{tr}\left(\rho\left[\sum_n e\mathcal{R}_{n\xi}, \sum_{n'}\frac{e\mathcal{V}_{n'\xi'}(t)}{\Omega}\right]\right),$$

where e is the electron charge, tr is a many-body trace, ρ is the equilibrium (many-body) density matrix, $\mathcal{R}_{n\xi}$ is the position in Cartesian direction ξ ($\xi = x, y, z$) of electron n, and $\mathcal{V}_{n\xi} \equiv \frac{\hbar}{m_e}\left(\frac{1}{i}\frac{\partial}{\partial\mathcal{R}_{n\xi}} - k_\xi\right)$ is the corresponding velocity (where $k_\xi = \frac{\pi}{2L_\xi}$ is the Baldereschi k-point). For non-interacting electrons, the response function reduces to a single electron expression (see Appendix (A)):

$$\phi_{\xi\xi'}(t) = \frac{4e^2}{\hbar\Omega}\Im\mathrm{Tr}\left(p_{\mu\beta}(\mathcal{H})\,\mathcal{R}_\xi\mathcal{V}_{\xi'}(t)\right), \tag{27}$$

where Tr is a single particle operator trace, $\mathcal{R}_\xi$ and $\mathcal{V}_{\xi'}$ are single electron position and velocity operators respectively, $p_{\mu\beta}(\mathcal{H})$ is the Fermi-Dirac distribution, and $\mathcal{H}$ is the single particle Hamiltonian (at the Baldereschi k-point), which we take from KS-DFT. We have also included a factor 2 due to spin-degeneracy. The use of such a static KS Hamiltonian, as opposed to the TDDFT description, is the central approximation of the Kubo-Greenwood theory.

For $\omega \neq 0$, we multiply and divide by $-i\omega$ the integral of Eq. (26), use the identity $-i\omega e^{-i\omega t} = \frac{d}{dt}e^{-i\omega t}$ and then

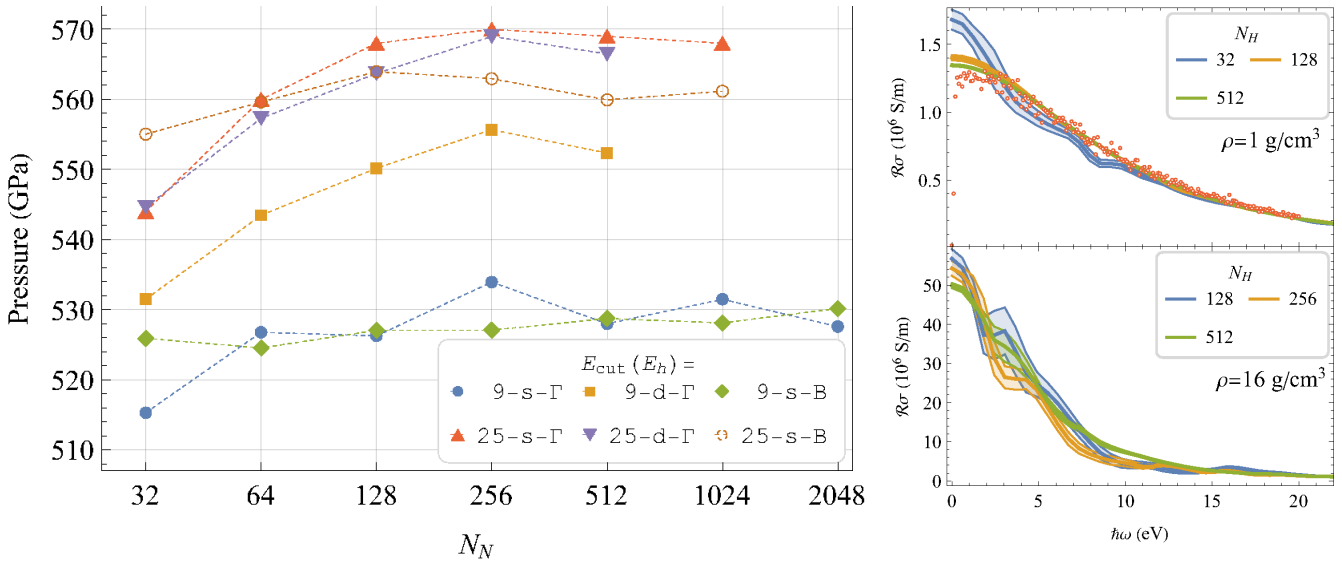

Figure 4. Pressure and conductivity averaged over a Langevin trajectory. **Left panel**: Size-dependence of pressure at density $1\,\mathrm{g/cm^3}$. Each point on the graph is an average over the pressure estimates along the xDFT (x="s" or "d") trajectory, performed using 9 or $25\,\mathrm{E_h}$ cutoff energy at the Γ or B (Baldereschi) k-point, as indicated in the legend. The sDFT calculations for each point on the Langevin trajectory used 40 stochastic orbitals at the LDA/NCPPs level. The dDFT calculations were performed by the VASP program [97–101], at the LDA/PAW level. The trajectory time-step was $\Delta\tau = 5$atu, and white noise parameter $\kappa^2 = 2$. **Right panels**: Size-dependence of the conductivity where the top (bottom) panel shows results for $\rho = 1\,(16)\,\mathrm{g/cm^3}$. Each conductivity curve is an average over the conductivity curves calculated for $N_s = 20$ configurations of the atomic nuclei (snapshots) taken every 1000 atu along the sDFT/Langevin trajectory. The error bars are $\pm s/\sqrt{N_s}$, where s is the standard deviation. One conductivity calculation produces an entire conductivity curve ($\sigma(\omega)$) based on 120 stochastic orbitals, performed at the Baldereschi k-point, with a $15E_h$ cutoff energy. Dark empty circles appearing in the top-right panel are conductivity calculations for H_{128} on the identical configurations using the deterministic conductivity method of Ref. [95] using VASP.

integrate by parts, obtaining

$$\sigma_{\xi\xi'}(\omega) = \frac{1}{i\omega}\left(-\phi_{\xi\xi'}(0) + \int_0^\infty \dot{\phi}_{\xi\xi'}(t)\, e^{-i\omega t} dt\right), \quad (28)$$

which involves the velocity-velocity response function:

$$\dot{\phi}_{\xi\xi'}(t) = -\frac{4e^2}{\hbar\Omega}\Im\mathrm{Tr}\left(p_{\mu\beta}(H)\,\mathcal{V}_\xi \mathcal{V}_{\xi'}(t)\right).$$

For evaluating the trace, we use the stochastic trace formula:

$$\mathrm{Tr}\left(p\mathcal{V}_\xi \mathcal{V}_{\xi'}(t)\right) = \mathbb{E}\left[\langle\zeta_{\xi t}|\mathcal{V}_{\xi'}|\eta_t\rangle\right], \quad (29)$$

where, for brevity, $p = p_{\beta\mu}(\mathcal{H})$ and

$$|\eta_t\rangle \equiv e^{-i\mathcal{H}t/\hbar}\sqrt{p}\,|\chi\rangle, \qquad |\zeta_{\xi t}\rangle \equiv e^{-i\mathcal{H}t/\hbar}\mathcal{V}_\xi\,|\eta\rangle,$$

and $|\chi\rangle$ is a stochastic state. To use Eq. (29) we generate a sample of N_s stochastic vectors χ, and for each, we obtain a specific value of $\langle\zeta_{\xi t}|\mathcal{V}_{\xi'}|\eta_t\rangle$. Averaging these values gives an estimate of the trace in the response function with a statistical error proportional to $1/\sqrt{N_s}$.

The trace operations provide correlation functions, which we denote $\dot{\phi}(t)$, (whether $\dot{\phi}_{\xi\xi'}(t)$ described above or $\dot{\psi}_{\xi\xi'}(t)$ described below). To use it for obtaining the conductivity as a function of ω, we first select a desired spectral energy resolution $\hbar\nu$, which defines a frequency grid $\omega_g = g \times \nu$, where $g = 0, 1, \ldots, N_\omega$, and then perform the Fourier integral of Eq. (28) for these frequencies. Given the resolution, the integral of the correlation function $\dot{\phi}(t)$ is augmented by a Gaussian window, discretized, and summed utilizing the fast-Fourier algorithm

$$\int_0^\infty \dot{\phi}(t)\, e^{-i\omega_g t} dt \to \int_0^\infty e^{-\frac{\nu^2 t^2}{2}} \dot{\phi}(t)\, e^{-i\omega_g t} dt \quad (30)$$
$$\to \frac{\tau_f}{N_\omega}\sum_{g'=0}^{N_\omega} w_{g'} e^{-\frac{\nu^2 \tau_{g'}^2}{2}} \dot{\phi}(\tau_{g'})\, e^{-i\omega_g \tau_{g'}}$$

on an equally spaced time-grid $\tau_g = g \times \frac{\tau_f}{N_\omega}$, extending from zero to $\tau_f = 7/\nu$. The number of time and frequency grid points is taken as $N_\omega = q_{\rm fac} \times \frac{E_{\rm cut}}{\hbar\nu}$, where the quality factor $q_{\rm fac} > 1$ determines the precision of the time integration. We also inserted integration weights, the simplest of which is the trapeze rule: $w_k = (1 - \delta_{k0}/2)$. These weights are essential as the integral is a half-Fourier transform, which means that the integrand does not decay smoothly to zero at the time-grid boundaries. We experimented with various choices of ν and q_{fac}, finding that a resolution of $\hbar\nu = 0.025\mathrm{E_h}$ and a quality factor in the range of 3 to 5 yield meaningful and stable results. Dividing these values by $i\omega_g$ ($g > 0$), we obtain the AC conductivity $\sigma_{\xi\xi'}(\omega_g)$.

Since evaluating the conductivity in Eq. (28) requires division of the Fourier integral by ω, the statistical fluctuations are amplified as $\omega \to 0$. The procedure is undefined for $\omega = 0$, the DC limit. In this case, we could use the analytical limit of Eq. (28),

$$\Re\sigma_{\xi\xi'}(0) = \int_0^\infty \dot{\phi}_{\xi\xi'}(t)\, t dt, \tag{31}$$

which does not divide by zero. We can use the same integration procedure outlined above for the integral. But experience shows that the stochastic error in Eq. (31), although finite, it is not small and requires extensive sampling. For the important case of $\xi = \xi'$ it is possible to show (see Appendix (B)) that

$$\Re\sigma_{\xi\xi}(0) = \int_0^\infty \dot{\psi}_{\xi\xi}(t)\, dt, \tag{32}$$

where (see Eq. (B4)):

$$\dot{\psi}_{\xi\xi}(t) = -\frac{2e^2}{\Omega}\Re\,\mathrm{Tr}\left(p'_{\mu\beta}(H)\,\mathcal{V}_\xi\mathcal{V}_\xi(t)\right),$$

and $p'_{\mu\beta}(\varepsilon) = -\beta p_{\mu\beta}(\varepsilon)(1 - p_{\mu\beta}(\varepsilon))$ is the derivative of the Fermi-Dirac function. The stochastic evaluation of the correlation function $\mathrm{Tr}\left(p'_{\mu\beta}(H)\,\mathcal{V}_\xi\mathcal{V}_\xi(t)\right)$ follows the same procedure as $\mathrm{Tr}\left(p_{\mu\beta}(H)\,\mathcal{V}_\xi\mathcal{V}_\xi(t)\right)$ except that this time we take $p = p'_{\beta\mu}(\mathcal{H})$. Then, the same time-integration scheme outlined above for the Fourier integral of $\dot{\phi}_{\xi\xi}$ can be used to evaluate the integral of Eq. (32).

The problem of high fluctuations in the low-frequency part of the AC conductivity is exacerbated due to the need to take smaller ν for converging the AC results to the DC limit: the smaller ν, the larger the fluctuations. Thus, we developed an interpolation procedure for the low-frequency spectrum relying on the steadiness of the DC conductivity. This procedure is described in Appendix C.

For calculating the direction-averaged conductivity, $\bar{\sigma} = \frac{1}{3}(\sigma_{xx} + \sigma_{yy} + \sigma_{zz})$, we replace the ξ component of the velocity ($\mathcal{V}_\xi$) in the above equations by a random-direction component $\mathcal{V}_d = \boldsymbol{\eta}^T\boldsymbol{V}$, where $\boldsymbol{\eta} = (\eta_x, \eta_y, \eta_z)$, taken as a *random point* on the 3D unit sphere. Since $\mathbb{E}\left[\boldsymbol{\eta}\boldsymbol{\eta}^T\right] = \frac{1}{3}\mathcal{I}$, where $\mathcal{I}$ is the 3×3 unit matrix. Averaging over $\mathcal{V}_d$ automatically computes $\bar{\sigma}$.

V. TEST CASE: HYDROGEN AT 30,000K

In this section, we use as a test case Hydrogen at 30,000K. We first consider system-size effects on the estimation of pressure and conductivity. Then, we give its equation of state, electric conductivity, and radial distributions, comparing, where possible, with VASP [97–101].

All sDFT calculations in this section used 40 stochastic orbitals (for all system sizes), the LDA exchange-correlation energy functional, and norm-conserving pseudopotentials [102]. Unless specifically mentioned otherwise, we use $9\mathrm{E_h}$ cutoff energy and the Baldereschi k-point [103].

A. System-size dependent pressure and conductivity

In Fig. 4 we present the pressure (left panel) and the conductivity (right panel) estimates for Hydrogen at 30,000K and density $\rho = 1\,\mathrm{g/cm^3}$, as a function of the system size. The pressure estimates at the Baldereschi k-point are rather steady and change only mildly with system size. Those done at the Γ point show a stronger sensitivity to system size, peaking at H_{256} and then decreasing towards the steadier k-point values. The sDFT pressure estimates increase by about 5% when going from cutoff energy of 9 to $25\mathrm{E_h}$. The dDFT results, based on the VASP code, are less sensitive to the cutoff energy and change by only 2.5%. This reflects the superiority of the PAWs used by VASP over the norm-conserving pseudopotentials used in the sDFT calculation when converging to the infinite energy cutoff limit. The sDFT and the VASP pressure estimates are similar at the higher cutoff energy.

The size dependence of Hydrogen conductivity at 30,000K, calculated at the Baldereschi k-point, is shown for two density values in the right panel of Fig. 4. For $1\,\mathrm{g/cm^3}$, the conductivity curves of $\mathrm{H_{128}}$ and $\mathrm{H_{512}}$ are already quite close (a difference of 3%). Note that the larger the system, the smaller the fluctuations. We also show results from a deterministic calculation on $\mathrm{H_{128}}$, which tend to be too small as ω decreases but fit our results well for all other frequencies.

Finally, the conductivity for the high-density systems is much more noisy than at low density, and the system size effects are more noticeable, since the simulation cell size is small for these systems.

B. Density-dependent properties of Hydrogen at 30,000K

The estimated pressure of Hydrogen at $T = 30,000K$ as a function of density is depicted for sDFT and dDFT (using VASP) in the left panel of Fig. 5. The two curves are generally close. The more significant difference in the lower-pressure estimates stems primarily from the smaller cutoff energy used in our calculation. The equation of state can be fitted by a van der Waals form, $P = P_{ideal}\left(1 + \frac{\rho}{\rho_0}\right)$ with $\rho_0 = 0.87\,\mathrm{g/cm^3}$.

The right panel of Fig. 5 illustrates the radial distribution for Hydrogen at $T = 30,000\mathrm{K}$, with varying densities from 0.25 to $16\,\mathrm{g/cm^3}$. At the lowest density, it reveals a relatively large excluded volume with some corrugated pattern. As the density increases to $1\,g/cm^3$, the radial distribution curve steepens as the proton-proton repulsion range shortens, and the corrugated pattern largely dies out, leaving a shallow signature of a correlation shell at $r = 1.5$ï¿œ. This feature is enhanced and contracts to a shorter distance of 0.75ï¿œ at the density of $4\,\mathrm{g/cm^3}$. In this regime, the radial distribution signifies a combined short-range repulsion and longer-range attraction

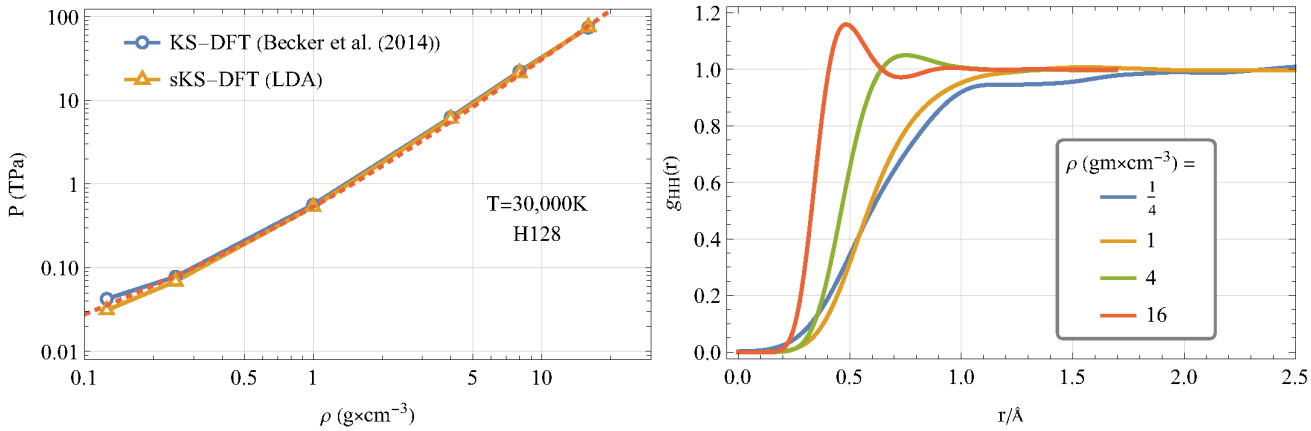

Figure 5. **Left panel**: the estimated pressure as a function of density for Hydrogen at $T = 30,000K$. The results of the sDFT calculations are shown together with the calculations taken from ref. [13] and a dotted van der Waals trend of $P(\rho) = \frac{\rho}{m_p} k_B T \left(1 + \frac{\rho}{\rho_0}\right)$, where $\rho_0 = 0.87\, g/cm^3$ is obtained by fitting. **Right panel**: the H-H radial distribution for different densities.

between pairs, typical of a gas. Finally, at the highest density considered, 16 g/cm^3, the correlation shell contracts further to 0.5ï¿œ while a second correlation shell seems to form 0.9ï¿œ, hence a radial distribution typical of a liquid emerges at these high densities.

We now turn to studying hydrogen conductivity using Drude's theory of metals [104] as reference point. Drude's theory gives the real part of the normalized conductivity at frequency ω as

$$\frac{\Re\sigma(\omega)}{n} = \frac{e^2}{m_e} \frac{\tau_c}{1+\omega^2\tau_c^2}, \tag{33}$$

where $n = \frac{N_e}{\Omega}$ is the average electron density, and τ_c, the collision time, is the only material parameter. τ_c is assumed independent of n. In Fig. 6 (left panel) we plot our stochastic estimates of the ab initio normalized conductivity for Hydrogen in various densities at 30,000K. While the normalized conductivity in Drude's theory (Eq. (33)) does not depend on n, the ab initio DC normalized conductivity does depend on it: it changes fourfold as n changes 64fold. Yet, as seen in Fig. 6, at $\hbar\omega = 7.2$eV, all four *ab initio* curves cross at approximately the same point, the *isosbestic point*, where they assume *the same* normalized conductivity value of $0.6 \times 10^{-3} \mathrm{Sa}_0^2$. The existence of the isosbestic point, especially in the rather large density range seen here is sometimes indicative of a system composed of two phases or two states [105–107]. The value of τ_c at the isosbestic point is equal to $(0.084 \pm 0.035i)$ fs, with the real part small relative to typical values of τ_c for room-temperature metals (between 1 and 10 fs [104]). This result is consistent with the dense metal (with r_s between 0.28 and 0.7) we have, and the high temperatures should speed up relaxation times and shorten mean free paths in the material. Eq. (33), also shows that $\Re\sigma$ is proportional to ω^{-2} for high frequencies, $\omega\tau_c \gg 1$ (in our case, $\hbar\omega > 30$eV). As seen in the inset of the figure, the ab initio conductivity decreases faster than the Drude second power law in the frequency.

The relative statistical errors in the conductivity evaluation (before stabilization according to the method of Appendix C) are shown in the right panel of the figure. In general, they grow with the density of the gas. Remarkably, the DC conductivity, calculated through Eq. (32), has a much smaller statistical error than the AC conductivity.

VI. SUMMARY

We developed a linear-scaling stochastic DFT implementation in periodic boundary conditions combined with Langevin dynamics, which we applied to Hydrogen at $30,000K$. Our pressure estimates at various Hydrogen densities between $0.125 - 16$ g/cm^3 matched well with results based on deterministic DFT for high cutoff energy (near convergence). The sensitivity to the cutoff energy reduced as the density increased.

The pair correlation functions showed that Hydrogen exhibits gas-like behavior at densities below 4 g/cm^3 and liquid-like behavior above it. We also developed a new stochastic method to estimate the Kubo-Greenwood conductivity with minimal statistical noise at $\omega \to 0$. All the calculations were done in the Baldereschi k-point, and then the overall size effects in the hydrogen systems were not large once H_{512} was used, except for the high density which required a large number of atoms.

Future work will focus on adapting stochastic time-dependent DFT [108–110] and Green's function methodologies [111–113] for WDM applications, building on the foundation of our current work.

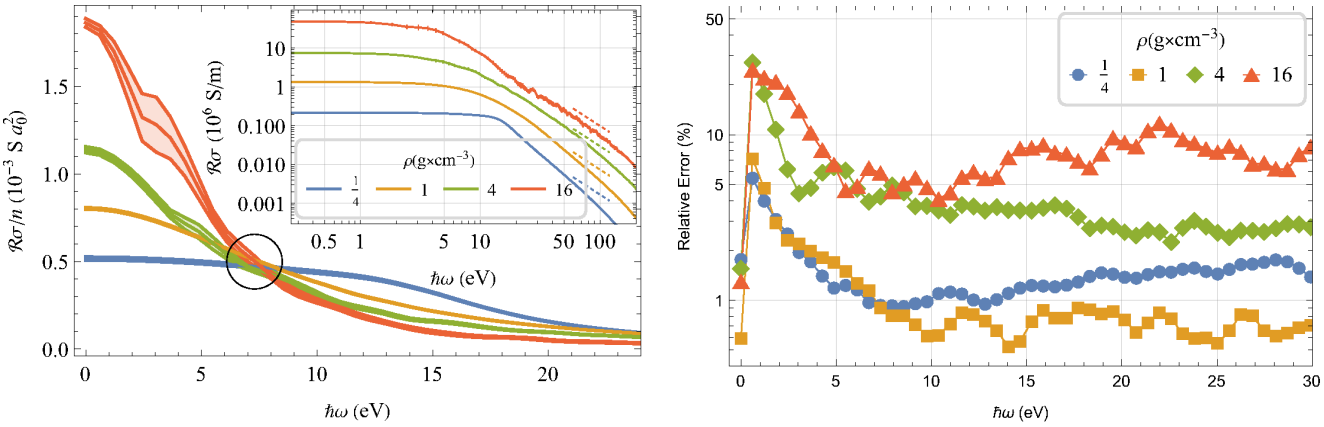

Figure 6. **Left panel**: The real part of the Kubo-Greenwood conductivity normalized by the electron density at $T = 30,000K$. The black circle indicates an *isosbestic point*, which appears at 7.2eV, where all systems have the same normalized conductivity of $\sim 0.5 \times 10^{-3}\, Sa_0^2$. The inset shows the conductivity in log-log scale, with dashed lines indicating slopes of ω^{-2}. **Right panel**: The relative error bars for the conductivity calculations, as described in the caption of Fig. 4.

Acknowledgment

RB and RR thank the German Israel Foundation for funding this project. ER acknowledges support from the Center for Computational Study of Excited-State Phenomena in Energy Materials (C2SEPEM) at the Lawrence Berkeley National Laboratory, funded by the U.S. Department of Energy, Office of Science, Basic Energy Sciences, Materials Sciences and Engineering Division, under Contract No. DE-AC02-05CH11231, as part of the Computational Materials Sciences Program.

Appendix A: Proof of Eq. (27)

For non-interacting electrons, the Hamiltonian and the grand canonical distribution are

$$H = \sum_i \varepsilon_i n_i, \qquad n_i \equiv a_i^\dagger a_i, \qquad N = \sum_i n_i, \qquad \rho = \frac{e^{-\beta(H-N\mu)}}{\mathrm{tr}\left[e^{-\beta(H-N\mu)}\right]}$$

where, a_i ($a_i^\dagger$) are electron annihilation (creation) operator into eigenstates of the Hamiltonian, with the standard anti commutation relations $\{a_i, a_j\} = \left\{a_i^\dagger, a_j^\dagger\right\} = 0$, $\left\{a_i a_j^\dagger\right\} = \delta_{ij}$.

From these relations alone we find the following:

$$\left[a_i^\dagger a_j, a_k^\dagger a_l\right] = \delta_{jk} a_i^\dagger a_l - \delta_{il} a_k^\dagger a_j, \tag{A1}$$

$$\mathrm{tr}\left[\rho a_i^\dagger a_l\right] = \delta_{il} \mathrm{tr}\left[\rho n_i\right] \equiv \delta_{il} p_{\mu\beta}\left(\varepsilon_i\right), \tag{A2}$$

and

$$e^{iHt} a_k^\dagger a_l e^{-iHt} = e^{-i(\varepsilon_l - \varepsilon_k)t} a_k^\dagger a_l. \tag{A3}$$

From Eqs. (A1) and (A2)

$$\mathrm{tr}\left[\rho\left[a_i^\dagger a_j, a_k^\dagger a_l\right]\right] = \left(p_{\mu\beta}^i - p_{\mu\beta}^j\right)\delta_{jk}\delta_{il}. \tag{A4}$$

and

$$\mathrm{tr}\left[\rho\left[a_i^\dagger a_j, a_k^\dagger\left(t\right) a_l\left(t\right)\right]\right] = e^{i(\varepsilon_i - \varepsilon_j)t/\hbar}\left(p_{\mu\beta}^i - p_{\mu\beta}^j\right)\delta_{jk}\delta_{il}. \tag{A5}$$

Therefore, first quantization (single-particle) observables $\mathcal{A}$ and $\mathcal{B}$, summed over all electrons $\mathcal{A} = \sum_n \mathcal{A}_n$ and $\mathcal{B} = \sum_n \mathcal{B}_n$ correspond, in second quantization, to $\hat{A} = a_i^\dagger a_j A^{ij}$ and $\hat{B} = a_i^\dagger a_j B^{ij}$ ($A^{ij} = \langle i\left|\mathcal{A}\right|j\rangle$ and $B^{ij} = \langle i\left|\mathcal{B}\right|j\rangle$). We find from Eq. (A4):

$$\mathrm{tr}\left[\rho\left[\hat{A}, \hat{B}\right]\right] = \mathrm{Tr}\left[p_{\mu\beta}\left(\mathcal{H}\right)\left[\mathcal{A}, \mathcal{B}\right]\right],$$

and from these:

$$\Im\,\mathrm{tr}\left[\rho\hat{A}\hat{B}\right] = \Im\,\mathrm{Tr}\left[p_{\mu\beta}\left(\mathcal{H}\right)\mathcal{A}\mathcal{B}\right]. \tag{A6}$$

Using Eq. (A3) we obtain the generalization of Eq. (A6)

$$\Im\,\mathrm{tr}\left[\rho\hat{A}\hat{B}\left(t\right)\right] = \Im\,\mathrm{Tr}\left[p_{\mu\beta}\left(\mathcal{H}\right)\mathcal{A}\mathcal{B}\left(t\right)\right]. \tag{A7}$$

This latter equation, used with $\hat{A} \to \sum_n \mathcal{R}_{n\xi}$ and $\hat{B} \to \sum_n \mathcal{V}_{n\xi'}$ gives Eq. (27).

Appendix B: Proof of Eq. (32)

The Fourier-transform of Eq. (A5) gives:

$$\int_{-\infty}^{\infty} e^{-i\omega t}\mathrm{tr}\left[\rho\left[a_i^\dagger a_j, e^{iHt}a_k^\dagger a_l e^{-iHt}\right]\right]dt = 2\pi\delta\left(\frac{\varepsilon_i-\varepsilon_j}{\hbar}+\omega\right)\left(p_{\mu\beta}\left(\varepsilon_j-\hbar\omega\right)-p_{\mu\beta}\left(\varepsilon_j\right)\right)\delta_{jk}\delta_{il},$$

where we used the spectral representation of Dirac delta functions, $2\pi\delta\left(\omega\right)=\int_{-\infty}^{\infty}e^{-i\omega t}dt$, and the identity $\delta\left(x-y\right)f\left(x\right)=\delta\left(x-y\right)f\left(y\right)$. Dividing the above expression by $i\omega$ and taking the limit $\omega\to 0$ we find:

$$\lim_{\omega\to 0}\frac{1}{i\omega}\int_{-\infty}^{\infty} e^{-i\omega t}\mathrm{tr}\left[\rho\left[a_i^\dagger a_j, e^{iHt}a_k^\dagger a_l e^{-iHt}\right]\right]dt = 2\pi\hbar i\delta\left(\frac{\varepsilon_i-\varepsilon_j}{\hbar}\right)p'_{\mu\beta}\left(\varepsilon_j\right)\delta_{jk}\delta_{il}.$$

Using the spectral representation in the reverse direction, we find:

$$\lim_{\omega\to 0}\frac{1}{i\omega}\int_{-\infty}^{\infty} e^{-i\omega t}\mathrm{tr}\left[\rho\left[a_i^\dagger a_j, e^{iHt}a_k^\dagger a_l e^{-iHt}\right]\right]dt = i\hbar\int_{-\infty}^{\infty} e^{-i(\varepsilon_i-\varepsilon_j)t}p'_{\mu\beta}\left(\varepsilon_j\right)dt\delta_{jk}\delta_{il}.$$

From these, it is now straightforward to show the two one-body observables

$$\lim_{\omega\to 0}\frac{1}{i\omega}\int_{-\infty}^{\infty} e^{-i\omega t}\mathrm{tr}\left[\rho\left[\hat{A},\hat{B}\left(t\right)\right]\right]dt = i\hbar\int_{-\infty}^{\infty}\mathrm{Tr}\left[p'_{\mu\beta}\left(\mathcal{H}\right)\mathcal{B}\left(t\right)\mathcal{A}\right]dt. \tag{B1}$$

For the case $A=B$, the left-hand side can be developed to give an integral over positive times

$$\lim_{\omega\to 0}\frac{1}{i\omega}\int_{-\infty}^{\infty} e^{-i\omega t}\mathrm{tr}\left[\rho\left[\hat{A},\hat{A}\left(t\right)\right]\right]dt = 4i\Re\left[\lim_{\omega\to 0}\frac{1}{i\omega}\int_{0}^{\infty} e^{-i\omega t}\Im\,\mathrm{tr}\left[\rho\hat{A}\hat{A}\left(t\right)\right]dt\right]. \tag{B2}$$

The right-hand side of Eq. (B1) can also be developed in a similar fashion:

$$i\hbar\int_{-\infty}^{\infty}\mathrm{Tr}\left[p'_{\mu\beta}\left(\mathcal{H}\right)\mathcal{A}\left(t\right)\mathcal{A}\right]dt = 2i\hbar\Re\int_{0}^{\infty}\mathrm{Tr}\left[p'_{\mu\beta}\left(\mathcal{H}\right)\mathcal{A}\mathcal{A}\left(t\right)\right]dt. \tag{B3}$$

Equating both right sides:

$$\Re\left[\lim_{\omega\to 0}\frac{1}{i\omega}\int_{0}^{\infty} e^{-i\omega t}\Im\,\mathrm{tr}\left[\rho\hat{A}\hat{A}\left(t\right)\right]dt\right] = \frac{\hbar}{2}\Re\int_{0}^{\infty}\mathrm{Tr}\left[p'_{\mu\beta}\left(\mathcal{H}\right)\mathcal{A}\mathcal{A}\left(t\right)\right]dt.$$

Finally, using Eq. (A7) we obtain:

$$\Re\left[\lim_{\omega\to 0}\frac{1}{i\omega}\int_{0}^{\infty} e^{-i\omega t}dt\Im\,\mathrm{tr}\left[p_{\mu\beta}\left(\mathcal{H}\right)\mathcal{A}\mathcal{A}\left(t\right)\right]\right] = \frac{\hbar}{2}\int_{0}^{\infty}\Re\,\mathrm{Tr}\left[p'_{\mu\beta}\left(\mathcal{H}\right)\mathcal{A}\mathcal{A}\left(t\right)\right]dt, \tag{B4}$$

from which Eq. (32) can be directly deduced.

Appendix C: Stabilizing the low-frequency conductivity spectrum

One of the practical problems in calculating the conductivity at low frequencies arises in connection with introducing a finite resolution parameter ν in Eq. 30. The finite resolution distorts and usually underestimates the conductivity. This is seen in the red empty dots of Fig. 4 which shows reduced conductivity as $\omega\to 0$.

A second problem involves the fact that our conductivity calculations use a stochastic approach, which has fluctuation errors. For the low-frequency these fluctuations grow considerably as $\omega\to 0$ (see right panel of Fig. 6) due to the division by ω in Eq. (28).

The two problems described above combine: the high fluctuations in the low-frequency part of the AC conductivity is exacerbated when we take smaller ν, needed for converging the AC results to the DC limit.

Here, we introduce an approximation that helps converge the low frequency AC conductivity, which relies on the fact that the DC conductivity ($\omega=0$), calculated by a different expression, Eq. (32), has finite and small fluctuations (seen in the right panel of Fig. 6). Our stabilization procedure mixes the low-frequency conductivity with that of an optimized model:

$$\sigma_k \leftarrow \left(1-w_k\right)\sigma_k + w_k\sigma_{\mathrm{model}}\left(\omega_k\right),$$

where σ_k is the conductivity corresponding to the fre-

quency $\omega_k = k\nu$, $k = 0, 1, 2, \ldots$. Here, w_k are mixing weights

$$w_k = \frac{1}{1 + \left(\frac{\omega_k}{\omega_c}\right)^6}.$$

Emphasizing the low-energy spectrum. Since our system exhibits a metallic behavior, we choose ω_c as the highest frequency in the spectrum for which $\sigma_c > 0.7\sigma_0$ and we use the Drude model $\sigma_{\text{model}}(\omega) = \frac{\sigma_0}{1+\omega^2\tau_c^2}$, depending on the single parameter τ_c, the collision time. Given the calculated spectrum, we set this parameter as follows:

$$\tau_c^2 = \frac{\sum_k w_k \omega_k^2 \sigma_k (\sigma_0 - \sigma_k)}{\sum_k w_k \omega_k^4 \sigma_k^2}.$$

This choice of parameter makes the calculated conductivity values σ_k as close as possible, in the root-mean-square sense to those of the model conductivity $\sigma_{\text{model}}(\omega_k)$, by minimizing the Lagrangian $L\left(\tau_c^2\right) = \sum_k w_k \left(\left(1 + \omega_k^2\tau_c^2\right)\sigma_k - \sigma_0\right)^2$.

[1] Tristan Guillot. Interiors of giant planets inside and outside the solar system. *science*, 286(5437):72–77, 1999. Publisher: American Association for the Advancement of Science.

[2] Jeffrey H. Nguyen and Neil C. Holmes. Melting of iron at the physical conditions of the Earth's core. *Nature*, 427(6972):339–342, January 2004. Number: 6972 Publisher: Nature Publishing Group.

[3] Ronald Redmer, Thomas R. Mattsson, Nadine Nettelmann, and Martin French. The phase diagram of water and the magnetic fields of Uranus and Neptune. *Icarus*, 211(1):798–803, January 2011.

[4] Monica Pozzo, Chris Davies, David Gubbins, and Dario AlfÃš. Thermal and electrical conductivity of iron at Earth's core conditions. *Nature*, 485(7398):355–358, May 2012.

[5] Alessandra Benuzzi-Mounaix, Stéphane Mazevet, Alessandra Ravasio, Tommaso Vinci, Adrien Denoeud, Michel Koenig, Nourou Amadou, Erik Brambrink, Floriane Festa, Anna Levy, Marion Harmand, Stéphanie Brygoo, Gael Huser, Vanina Recoules, Johan Bouchet, Guillaume Morard, François Guyot, Thibaut De Resseguier, Kohei Myanishi, Norimasa Ozaki, Fabien Dorchies, Jerôme Gaudin, Pierre Marie Leguay, Olivier Peyrusse, Olivier Henry, Didier Raffestin, Sebastien Le Pape, Ray Smith, and Riccardo Musella. Progress in warm dense matter study with applications to planetology. *Phys. Scr.*, T161:014060, May 2014.

[6] Martin French and Nadine Nettelmann. Viscosity and Prandtl Number of Warm Dense Water as in Ice Giant Planets. *ApJ*, 881(1):81, August 2019.

[7] David Ehrenreich, Christophe Lovis, Romain Allart, María Rosa Zapatero Osorio, Francesco Pepe, Stefano Cristiani, Rafael Rebolo, Nuno C. Santos, Francesco Borsa, Olivier Demangeon, Xavier Dumusque, Jonay I. González Hernández, Nũria Casasayas-Barris, Damien Ségransan, Sérgio Sousa, Manuel Abreu, Vardan Adibekyan, Michael Affolter, Carlos Allende Prieto, Yann Alibert, Matteo Aliverti, David Alves, Manuel Amate, Gerardo Avila, Veronica Baldini, Timothy Bandy, Willy Benz, Andrea Bianco, Emeline Bolmont, FranÃ§ois Bouchy, Vincent Bourrier, Christopher Broeg, Alexandre Cabral, Giorgio Calderone, Enric Pallé, H. M. Cegla, Roberto Cirami, João M. P. Coelho, Paolo Conconi, Igor Coretti, Claudio Cumani, Guido Cupani, Hans Dekker, Bernard Delabre, Sebastian Deiries, Valentina D'Odorico, Paolo Di Marcantonio, Pedro Figueira, Ana Fragoso, Ludovic Genolet, Matteo Genoni, Ricardo Génova Santos, Nathan Hara, Ian Hughes, Olaf Iwert, Florian Kerber, Jens Knudstrup, Marco Landoni, Baptiste Lavie, Jean-Louis Lizon, Monika Lendl, Gaspare Lo Curto, Charles Maire, Antonio Manescau, C. J. a. P. Martins, Denis Mégevand, Andrea Mehner, Giusi Micela, Andrea Modigliani, Paolo Molaro, Manuel Monteiro, Mario Monteiro, Manuele Moschetti, Eric Müller, Nelson Nunes, Luca Oggioni, António Oliveira, Giorgio Pariani, Luca Pasquini, Ennio Poretti, José Luis Rasilla, Edoardo Redaelli, Marco Riva, Samuel Santana Tschudi, Paolo Santin, Pedro Santos, Alex Segovia Milla, Julia V. Seidel, Danuta Sosnowska, Alessandro Sozzetti, Paolo Spanó, Alejandro Suárez Mascareõo, Hugo Tabernero, Fabio Tenegi, Stéphane Udry, Alessio Zanutta, and Filippo Zerbi. Nightside condensation of iron in an ultrahot giant exoplanet. *Nature*, 580(7805):597–601, April 2020. Number: 7805 Publisher: Nature Publishing Group.

[8] Jonathan J. Fortney and Nadine Nettelmann. The Interior Structure, Composition, and Evolution of Giant Planets. *Space Sci Rev*, 152(1-4):423–447, May 2010.

[9] M. Bethkenhagen, E. R. Meyer, S. Hamel, N. Nettelmann, M. French, L. Scheibe, C. Ticknor, L. A. Collins, J. D. Kress, J. J. Fortney, and R. Redmer. Planetary Ices and the Linear Mixing Approximation. *ApJ*, 848(1):67, October 2017.

[10] Martin French, Andreas Becker, Winfried Lorenzen, Nadine Nettelmann, Mandy Bethkenhagen, Johannes Wicht, and Ronald Redmer. *Ab initio* simulations for the material properties along jupiter's adiabat. *Astrophys. J. Suppl. Ser.*, 202:5, 2012.

[11] Didier Saumon, William B. Hubbard, Gilles Chabrier, and Hugh M. van Horn. The Role of the Molecular-metallic Transition of Hydrogen in the Evolution of Jupiter, Saturn, and Brown Dwarfs. *ApJ*, 391:827, June 1992. ADS Bibcode: 1992ApJ...391..827S.

[12] S. R. Kulkarni. Brown Dwarfs: A Possible Missing Link Between Stars and Planets. *Science*, 276(5317):1350–1354, May 1997. Publisher: American Association for the Advancement of Science.

[13] Andreas Becker, Winfried Lorenzen, Jonathan J. Fortney, Nadine Nettelmann, Manuel Schöittler, and Ronald Redmer. Ab initio equations of state for hydrogen (H-REOS.3) and helium (He-REOS.3) and their implications for the interior of brown dwarfs. *ApJS*, 215(2):21, December 2014.

[14] N. Booth, A. P. L. Robinson, P. Hakel, R. J. Clarke, R. J. Dance, D. Doria, L. A. Gizzi, G. Gregori, P. Koester, L. Labate, T. Levato, B. Li, M. Makita, R. C. Mancini, J. Pasley, P. P. Rajeev, D. Riley, E. Wagenaars, J. N. Waugh, and N. C. Woolsey. Laboratory measurements of resistivity in warm dense plasmas relevant to the microphysics of brown dwarfs. *Nat Commun*, 6(1):8742, November 2015.

[15] Andreas Becker, Mandy Bethkenhagen, Clemens Kellermann, Johannes Wicht, and Ronald Redmer. Material Properties for the Interiors of Massive Giant Planets and Brown Dwarfs. *AJ*, 156(4):149, September 2018.

[16] Gilles Chabrier. Quantum Effects in Dense Coulombic Matter: Application to the Cooling of White Dwarfs. *ApJ*, 414:695, September 1993. ADS Bibcode: 1993ApJ...414..695C.

[17] Didier Saumon, Simon Blouin, and Pier-Emmanuel Tremblay. Current challenges in the physics of white dwarf stars. *Physics Reports*, 988:1–63, November 2022.

[18] D. E. Hinkel. Scientific and technological advancements in inertial fusion energy. *Nucl. Fusion*, 53(10):104027, September 2013. Publisher: IOP Publishing and International Atomic Energy Agency.

[19] John Lindl. Development of the indirect-drive approach to inertial confinement fusion and the target physics basis for ignition and gain. *Physics of Plasmas*, 2(11):3933–4024, November 1995.

[20] E.M. Campbell, V.N. Goncharov, T.C. Sangster, S.P. Regan, P.B. Radha, R. Betti, J.F. Myatt, D.H. Froula, M.J. Rosenberg, I.V. Igumenshchev, W. Seka, A.A. Solodov, A.V. Maximov, J.A. Marozas, T.J.B. Collins, D. Turnbull, F.J. Marshall, A. Shvydky, J.P. Knauer, R.L. McCrory, A.B. Sefkow, M. Hohenberger, P.A. Michel, T. Chapman, L. Masse, C. Goyon, S. Ross, J.W. Bates, M. Karasik, J. Oh, J. Weaver, A.J. Schmitt, K. Obenschain, S.P. Obenschain, S. Reyes, and B. Van Wonterghem. Laser-direct-drive program: Promise, challenge, and path forward. *Matter and Radiation at Extremes*, 2(2):37–54, March 2017.

[21] BA Remington, RM Cavallo, MJ Edwards, DD-M Ho, BF Lasinski, KT Lorenz, HE Lorenzana, JM McNaney, SM Pollaine, and RF Smith. Accessing high pressure states relevant to core conditions in the giant planets. *High Energy Density Laboratory Astrophysics*, pages 235–240, 2005. Publisher: Springer.

[22] Katerina Falk. Experimental methods for warm dense matter research. *High Pow Laser Sci Eng*, 6:e59, 2018.

[23] B. Militzer, D. M. Ceperley, J. D. Kress, J. D. Johnson, L. A. Collins, and S. Mazevet. Calculation of a Deuterium Double Shock Hugoniot from *Ab Initio* Simulations. *Phys. Rev. Lett.*, 87(27):275502, December 2001.

[24] Bastian Holst, Ronald Redmer, and Michael P. Desjarlais. Thermophysical properties of warm dense hydrogen using quantum molecular dynamics simulations. *Phys. Rev. B*, 77(18):184201, May 2008.

[25] Miguel A. Morales, Carlo Pierleoni, and D. M. Ceperley. Equation of state of metallic hydrogen from coupled electron-ion Monte Carlo simulations. *Phys. Rev. E*, 81(2):021202, February 2010.

[26] Ethan Brown, Miguel A. Morales, Carlo Pierleoni, and David Ceperley. Quantum Monte Carlo Techniques and Applications for Warm Dense Matter. In Frank Graziani, Michael P. Desjarlais, Ronald Redmer, and Samuel B. Trickey, editors, *Frontiers and Challenges in Warm Dense Matter*, pages 123–149. Springer International Publishing, Cham, 2014.

[27] Mandy Bethkenhagen, Bastian B. L. Witte, Maximilian Schörner, Gerd Röpke, Tilo Döppner, Dominik Kraus, Siegfried H. Glenzer, Philip A. Sterne, and Ronald Redmer. Carbon ionization at gigabar pressures: An *ab initio* perspective on astrophysical high-density plasmas. *Phys. Rev. Research*, 2(2):023260, June 2020.

[28] Mark Tuckerman. *Statistical Mechanics: Theory and Molecular Simulation*. OUP Oxford, February 2010. Google-Books-ID: Lo3Jqc0pgrcC.

[29] Hongwei Niu, Yubo Yang, Scott Jensen, Markus Holzmann, Carlo Pierleoni, and David M. Ceperley. Stable Solid Molecular Hydrogen above 900 K from a Machine-Learned Potential Trained with Diffusion Quantum Monte Carlo. *Phys. Rev. Lett.*, 130(7):076102, February 2023.

[30] Chris J. Pickard and Richard J. Needs. Structure of phase III of solid hydrogen. *Nature Phys*, 3(7):473–476, July 2007.

[31] Klaus-Peter Bohnen, Miguel Kiwi, and Harry Suhl. Friction Coefficient of an Adsorbed H Atom on a Metal Surface. *Phys. Rev. Lett.*, 34(24):1512–1515, June 1975.

[32] M P Grumbach, D Hohl, R M Martin, and R Car. Ab initio molecular dynamics with a finite-temperature density functional. *J. Phys.: Condens. Matter*, 6(10):1999–2014, March 1994.

[33] B. Hellsing and M. Persson. Electronic Damping of Atomic and Molecular Vibrations at Metal Surfaces. *Phys. Scr.*, 29(4):360, April 1984.

[34] Roi Baer and Nidal Siam. Real-time study of the adiabatic energy loss in an atomic collision with a metal cluster. *J. Chem. Phys.*, 121(13):6341–6345, 2004.

[35] Federico Becca and Sandro Sorella. *Quantum Monte Carlo Approaches for Correlated Systems*. Cambridge University Press, 1 edition, November 2017.

[36] Valentin V Karasiev, Travis Sjostrom, Debajit Chakraborty, James Dufty, Keith Runge, Frank E Harris, and Samuel B Trickey. Innovations in finite-temperature density functionals. In *Frontiers and Challenges in Warm Dense Matter*, volume 96 of *Lecture Notes in Computational Science and Engineering*. Springer Science & Business, 2014.

[37] P. Geerlings, F. De Proft, and W. Langenaeker. Conceptual Density Functional Theory. *Chem. Rev.*, 103(5):1793–1874, 2003.

[38] Richard M. Martin. *Electronic Structure: Basic Theory and Practical Methods*. Cambridge University Press, Cambridge UK, 2004.

[39] Jürg Hutter. Car-Parrinello molecular dynamics. *Wiley Interdisciplinary Reviews: Computational Molecular Science*, 2(4):604–612, 2012.

[40] Aurora Pribram-Jones, David A. Gross, and Kieron Burke. DFT: A Theory Full of Holes? *Annu. Rev. Phys. Chem.*, 66(1):283–304, April 2015.

[41] Richard M. Martin, Lucia Reining, and David M. Ceperley. *Interacting Electrons*. Cambridge University Press, June 2016. Google-Books-ID: ch1CDAAAQBAJ.

[42] Frank Jensen. *Introduction to computational chemistry*. Wiley, Chichester, UK ; Hoboken, NJ, third edition edition, 2017.

[43] O. Anatole von Lilienfeld, Klaus-Robert MÃŒller, and Alexandre Tkatchenko. Exploring chemical compound space with quantum-based machine learning. *Nat Rev*

Chem, 4(7):347–358, July 2020.

[44] John P. Perdew and Mel Levy. Physical Content of the Exact Kohn-Sham Orbital Energies: Band Gaps and Derivative Discontinuities. *Phys. Rev. Lett.*, 51(20):1884–1887, November 1983. Publisher: American Physical Society.

[45] Leeor Kronik, Tamar Stein, Sivan Refaely-Abramson, and Roi Baer. Excitation Gaps of Finite-Sized Systems from Optimally Tuned Range-Separated Hybrid Functionals. *J. Chem. Theory Comput.*, 8(5):1515–1531, 2012.

[46] N D Mermin. Thermal properties of the inhomogeneous electron gas. *Phys. Rev.*, 137(5):A1441, 1965.

[47] S. Pittalis, C. R. Proetto, A. Floris, A. Sanna, C. Bersier, K. Burke, and E. K. U. Gross. Exact Conditions in Finite-Temperature Density-Functional Theory. *Phys. Rev. Lett.*, 107(16):163001, 2011.

[48] Aurora Pribram-Jones, Stefano Pilatis, Eberhard K. U Gross, and Kieron Burke. Thermal Density Functional Theory in Context. In *Frontiers and Challenges in Warm Dense Matter*, volume 96 of *Lecture Notes in Computational Science and Engineering*. Springer Science & Business, 2014.

[49] Simon Groth, Tobias Dornheim, Travis Sjostrom, Fionn D. Malone, W. M. C. Foulkes, and Michael Bonitz. Ab initio Exchange-Correlation Free Energy of the Uniform Electron Gas at Warm Dense Matter Conditions. *Phys. Rev. Lett.*, 119(13):135001, September 2017.

[50] M Bonitz, T Dornheim, Zh A Moldabekov, S Zhang, P Hamann, H Kählert, A Filinov, K Ramakrishna, and J Vorberger. Ab initio simulation of warm dense matter. *Phys. Plasmas*, 27(4), 2020. Publisher: AIP Publishing.

[51] Zhandos Moldabekov, Tobias Dornheim, Jan Vorberger, and Attila Cangi. Benchmarking exchange-correlation functionals in the spin-polarized inhomogeneous electron gas under warm dense conditions. *Phys. Rev. B*, 105(3):035134, January 2022.

[52] Shen Zhang, Hongwei Wang, Wei Kang, Ping Zhang, and X. T. He. Extended application of Kohn-Sham first-principles molecular dynamics method with plane wave approximation at high energy—From cold materials to hot dense plasmas. *Physics of Plasmas*, 23(4):042707, April 2016.

[53] A. Blanchet, J. Clérouin, M. Torrent, and F. Soubiran. Extended first-principles molecular dynamics model for high temperature simulations in the Abinit code: Application to warm dense aluminum. *Computer Physics Communications*, 271:108215, February 2022.

[54] R. P. Feynman, N. Metropolis, and E. Teller. Equations of State of Elements Based on the Generalized Fermi-Thomas Theory. *Physical Review*, 75(10):1561–1573, May 1949. Publisher: American Physical Society.

[55] F. Perrot. Gradient correction to the statistical electronic free energy at nonzero temperatures: Application to equation-of-state calculations. *Physical Review A*, 20(2):586–594, August 1979. Publisher: American Physical Society.

[56] Valentin V Karasiev, Travis Sjostrom, and SB Trickey. Generalized-gradient-approximation noninteracting free-energy functionals for orbital-free density functional calculations. *Phys. Rev. B*, 86(11):115101, 2012.

[57] Travis Sjostrom and Jérôme Daligault. Fast and Accurate Quantum Molecular Dynamics of Dense Plasmas Across Temperature Regimes. *Phys. Rev. Lett.*, 113(15):155006, October 2014.

[58] Valentin V. Karasiev, Debajit Chakraborty, Olga A. Shukruto, and S. B. Trickey. Nonempirical generalized gradient approximation free-energy functional for orbital-free simulations. *Physical Review B*, 88(16):161108, October 2013. Publisher: American Physical Society.

[59] K. Luo, V. V. Karasiev, and S. B. Trickey. Towards accurate orbital-free simulations: A generalized gradient approximation for the noninteracting free energy density functional. *Physical Review B*, 101(7):075116, February 2020. Publisher: American Physical Society.

[60] Vincent L Ligneres and Emily A Carter. An introduction to orbital-free density functional theory. In Yip, S, editor, *Handbook of Materials Modeling,*, pages 137–148. Springer, The Netherlands, 2005.

[61] Flavien Lambert, Jean Clérouin, and Gilles Zérah. Very-high-temperature molecular dynamics. *Phys. Rev. E*, 73(1):016403, January 2006. Publisher: American Physical Society.

[62] Christopher Ticknor, Joel D. Kress, Lee A. Collins, Jean Clérouin, Philippe Arnault, and Alain Decoster. Transport properties of an asymmetric mixture in the dense plasma regime. *Phys. Rev. E*, 93(6):063208, June 2016. Publisher: American Physical Society.

[63] S. X. Hu, R. Gao, Y. Ding, L. A. Collins, and J. D. Kress. First-principles equation-of-state table of silicon and its effects on high-energy-density plasma simulations. *Phys. Rev. E*, 95(4):043210, April 2017.

[64] Alexander J. White, Ondrej Certik, Y. H. Ding, S. X. Hu, and Lee A. Collins. Time-dependent orbital-free density functional theory for electronic stopping power: Comparison to the Mermin-Kohn-Sham theory at high temperatures. *Phys. Rev. B*, 98(14):144302, October 2018. Publisher: American Physical Society.

[65] A. J. White, C. Ticknor, E. R. Meyer, J. D. Kress, and L. A. Collins. Multicomponent mutual diffusion in the warm, dense matter regime. *Phys. Rev. E*, 100(3):033213, September 2019.

[66] Wenhui Mi, Kai Luo, S. B. Trickey, and Michele Pavanello. Orbital-Free Density Functional Theory: An Attractive Electronic Structure Method for Large-Scale First-Principles Simulations. *Chem. Rev.*, page acs.chemrev.2c00758, October 2023.

[67] Bingqing Cheng, Guglielmo Mazzola, Chris J. Pickard, and Michele Ceriotti. Evidence for supercritical behaviour of high-pressure liquid hydrogen. *Nature*, 585(7824):217–220, September 2020.

[68] O. Anatole von Lilienfeld and Kieron Burke. Retrospective on a decade of machine learning for chemical discovery. *Nat Commun*, 11(1):4895, December 2020.

[69] Valentin V. Karasiev, Joshua Hinz, S. X. Hu, and S. B. Trickey. On the liquid–liquid phase transition of dense hydrogen. *Nature*, 600(7889):E12–E14, December 2021.

[70] J. A. Ellis, L. Fiedler, G. A. Popoola, N. A. Modine, J. A. Stephens, A. P. Thompson, A. Cangi, and S. Rajamanickam. Accelerating finite-temperature Kohn-Sham density functional theory with deep neural networks. *Phys. Rev. B*, 104(3):035120, July 2021.

[71] Bingqing Cheng, Sebastien Hamel, and Mandy Bethkenhagen. Thermodynamics of diamond formation from hydrocarbon mixtures in planets. *Nat Commun*,

14(1):1104, February 2023. Number: 1 Publisher: Nature Publishing Group.

[72] Roi Baer, Daniel Neuhauser, and Eran Rabani. Self-Averaging Stochastic Kohn-Sham Density-Functional Theory. *Phys. Rev. Lett.*, 111(10):106402, September 2013.

[73] Yael Cytter, Eran Rabani, Daniel Neuhauser, and Roi Baer. Stochastic Density Functional Theory at Finite Temperatures. *Phys. Rev. B*, 97:115207, 2018.

[74] Yael Cytter, Eran Rabani, Daniel Neuhauser, Martin Preising, Ronald Redmer, and Roi Baer. Transition to metallization in warm dense helium-hydrogen mixtures using stochastic density functional theory within the Kubo-Greenwood formalism. *Phys. Rev. B*, 100(19):195101, November 2019.

[75] A. J. White and L. A. Collins. Fast and Universal Kohn-Sham Density Functional Theory Algorithm for Warm Dense Matter to Hot Dense Plasma. *Phys. Rev. Lett.*, 125(5):055002, July 2020.

[76] Ming Chen, Roi Baer, Daniel Neuhauser, and Eran Rabani. Stochastic density functional theory: Real- and energy-space fragmentation for noise reduction. *J. Chem. Phys.*, 154(20):204108, May 2021.

[77] Roi Baer, Daniel Neuhauser, and Eran Rabani. Stochastic Vector Techniques in Ground-State Electronic Structure. *Annu. Rev. Phys. Chem.*, 73(1):12.1–12.18, April 2022.

[78] Tao Chen, Qianrui Liu, Yu Liu, Liang Sun, and Mohan Chen. Combining stochastic density functional theory with deep potential molecular dynamics to study warm dense matter, June 2023. arXiv:2306.01637 [physics].

[79] P. Hohenberg and W. Kohn. Inhomogeneous Electron Gas. *Phys. Rev.*, 136(3B):B864–B871, November 1964.

[80] W. Kohn and L. J. Sham. Self-Consistent Equations Including Exchange and Correlation Effects. *Phys. Rev.*, 140(4A):A1133–A1138, November 1965.

[81] Nathan Argaman and Guy Makov. Thermodynamics as an alternative foundation for zero-temperature density-functional theory and spin-density-functional theory. *Phys. Rev. B*, 66(5):052413, August 2002.

[82] M. Weinert and J. W. Davenport. Fractional occupations and density-functional energies and forces. *Phys. Rev. B*, 45(23):13709–13712, June 1992.

[83] Valentin V Karasiev, Travis Sjostrom, James Dufty, and SB Trickey. Accurate homogeneous electron gas exchange-correlation free energy for local spin-density calculations. *Phys. Rev. Lett.*, 112(7):076403, 2014.

[84] Valentin V. Karasiev, Lázaro Calderín, and S. B. Trickey. Importance of finite-temperature exchange correlation for warm dense matter calculations. *Physical Review E*, 93(6):063207, June 2016. Publisher: American Physical Society.

[85] Valentin V. Karasiev, James W. Dufty, and S. B. Trickey. Nonempirical Semilocal Free-Energy Density Functional for Matter under Extreme Conditions. *Physical Review Letters*, 120(7):076401, February 2018. Publisher: American Physical Society.

[86] Kushal Ramakrishna, Tobias Dornheim, and Jan Vorberger. Influence of finite temperature exchange-correlation effects in hydrogen. *Physical Review B*, 101(19):195129, May 2020. Publisher: American Physical Society.

[87] Joshua Hinz, Valentin V. Karasiev, S. X. Hu, Mohamed Zaghoo, Daniel Mejía-Rodríguez, S. B. Trickey, and L. Calderín. Fully consistent density functional theory determination of the insulator-metal transition boundary in warm dense hydrogen. *Physical Review Research*, 2(3):032065, September 2020. Publisher: American Physical Society.

[88] Valentin V. Karasiev, D. I. Mihaylov, and S. X. Hu. Meta-GGA exchange-correlation free energy density functional to increase the accuracy of warm dense matter simulations. *Physical Review B*, 105(8):L081109, February 2022. Publisher: American Physical Society.

[89] R. Kosloff. Time-Dependent Quantum-Mechanical Methods for Molecular- Dynamics. *J. Phys. Chem.*, 92(8):2087–2100, 1988.

[90] T. J. Rivlin. *Chebyshev Polynomials: From approximation Theory to Algebra and Numbers Theory*. Wiley, New-York, 1990.

[91] Ming Chen, Roi Baer, Daniel Neuhauser, and Eran Rabani. Energy window stochastic density functional theory. *J. Chem. Phys.*, 151(11):114116, September 2019.

[92] Ye Luo, Andrea Zen, and Sandro Sorella. Ab initio molecular dynamics with noisy forces: Validating the quantum Monte Carlo approach with benchmark calculations of molecular vibrational properties. *J. Chem. Phys.*, 141(19):194112, 2014.

[93] Ryogo Kubo. Statistical-Mechanical Theory of Irreversible Processes. I. General Theory and Simple Applications to Magnetic and Conduction Problems. *J. Phys. Soc. Jpn.*, 12(6):570–586, June 1957.

[94] D A Greenwood. The Boltzmann Equation in the Theory of Electrical Conduction in Metals. *Proc. Phys. Soc.*, 71(4):585–596, April 1958.

[95] Bastian Holst, Martin French, and Ronald Redmer. Electronic transport coefficients from ab initio simulations and application to dense liquid hydrogen. *Phys. Rev. B*, 83(23):235120, June 2011.

[96] L. Calderín, V. V. Karasiev, and S. B. Trickey. Kubo-Greenwood electrical conductivity formulation and implementation for projector augmented wave datasets. *Computer Physics Communications*, 221:118–142, December 2017.

[97] Georg Kresse and Jürgen Hafner. Ab initio molecular dynamics for liquid metals. *Phys. Rev. B*, 47(1):558, 1993.

[98] G. Kresse and J. Hafner. Ab initio molecular-dynamics simulation of the liquid-metal–amorphous-semiconductor transition in germanium. *Phys. Rev. B*, 49(20):14251–14269, May 1994. Publisher: American Physical Society.

[99] G. Kresse and J. Furthmüller. Efficient iterative schemes for *ab initio* total-energy calculations using a plane-wave basis set. *Phys. Rev. B*, 54(16):11169–11186, October 1996.

[100] Georg Kresse and Jürgen Furthmüller. Efficiency of ab-initio total energy calculations for metals and semiconductors using a plane-wave basis set. *Computational Materials Science*, 6(1):15–50, 1996.

[101] G. Kresse and D. Joubert. From ultrasoft pseudopotentials to the projector augmented-wave method. *Phys. Rev. B*, 59(3):1758–1775, January 1999. Publisher: American Physical Society.

[102] N. Troullier and J. L. Martins. Efficient Pseudopotentials for Plane-Wave Calculations. *Phys. Rev. B*, 43(3):1993–2006, 1991.

[103] A. Baldereschi. Mean-Value Point in the Brillouin Zone.

Phys. Rev. B, 7(12):5212–5215, June 1973.

[104] Neil W. Ashcroft and N. David Mermin. *Solid State Physics*. Orlandao, 1976.

[105] G. Wilse Robinson, Chul Hee Cho, and Jacob Urquidi. Isosbestic points in liquid water: Further strong evidence for the two-state mixture model. *The Journal of Chemical Physics*, 111(2):698–702, July 1999.

[106] M. Eckstein, M. Kollar, and D. Vollhardt. Isosbestic points in the spectral function of correlated electrons. *J Low Temp Phys*, 147(3-4):279–293, March 2007. arXiv:cond-mat/0609464.

[107] Paolo Renati, Zoltan Kovacs, Antonella De Ninno, and Roumiana Tsenkova. Temperature dependence analysis of the NIR spectra of liquid water confirms the existence of two phases, one of which is in a coherent state. *Journal of Molecular Liquids*, 292:111449, October 2019.

[108] Yi Gao, Daniel Neuhauser, Roi Baer, and Eran Rabani. Sublinear scaling for time-dependent stochastic density functional theory. *J. Chem. Phys.*, 142(3):034106, January 2015.

[109] Vojtěch Vlček, Roi Baer, and Daniel Neuhauser. Stochastic time-dependent DFT with optimally tuned range-separated hybrids: Application to excitonic effects in large phosphorene sheets. *J. Chem. Phys.*, 150(18):184118, May 2019.

[110] Xu Zhang, Gang Lu, Roi Baer, Eran Rabani, and Daniel Neuhauser. Linear-Response Time-Dependent Density Functional Theory with Stochastic Range-Separated Hybrids. *J. Chem. Theory Comput.*, 16(2):1064–1072, February 2020.

[111] Daniel Neuhauser, Yi Gao, Christopher Arntsen, Cyrus Karshenas, Eran Rabani, and Roi Baer. Breaking the Theoretical Scaling Limit for Predicting Quasiparticle Energies: The Stochastic G W Approach. *Phys. Rev. Lett.*, 113(7):076402, August 2014.

[112] Eran Rabani, Roi Baer, and Daniel Neuhauser. Time-dependent stochastic Bethe-Salpeter approach. *Phys. Rev. B*, 91(23):235302, June 2015.

[113] Daniel Neuhauser, Roi Baer, and Dominika Zgid. Stochastic self-consistent second-order Green‘s function method for correlation energies of large electronic systems. *J. Chem. Theory Comput.*, 13:5396–5403, 2017.